INL/JOU-21-61443-Revision-0

Burnable Absorbers in Nuclear Reactors - A Review

May 2022

Jordan Andrew Evans, Dennis D Keiser Jr, Mark D DeHart, Kevan D Weaver

Changing the World's Energy Future

INL is a U.S. Department of Energy National Laboratory operated by Battelle Energy Alliance, LLC

DISCLAIMER

This information was prepared as an account of work sponsored by an agency of the U.S. Government. Neither the U.S. Government nor any agency thereof, nor any of their employees, makes any warranty, expressed or implied, or assumes any legal liability or responsibility for the accuracy, completeness, or usefulness, of any information, apparatus, product, or process disclosed, or represents that its use would not infringe privately owned rights. References herein to any specific commercial product, process, or service by trade name, trade mark, manufacturer, or otherwise, does not necessarily constitute or imply its endorsement, recommendation, or favoring by the U.S. Government or any agency thereof. The views and opinions of authors expressed herein do not necessarily state or reflect those of the U.S. Government or any agency thereof.

INL/JOU-21-61443-Revision-0

Burnable Absorbers in Nuclear Reactors - A Review

Jordan Andrew Evans, Dennis D Keiser Jr, Mark D DeHart, Kevan D Weaver

May 2022

Idaho National Laboratory
Idaho Falls, Idaho 83415

http://www.inl.gov

Prepared for the
U.S. Department of Energy
Under DOE Idaho Operations Office
Contract DE-AC07-05ID14517

Burnable Absorbers in Nuclear Reactors – A Review

Jordan A. Evans[a*], Mark D. DeHart[a], Kevan D. Weaver[a], Dennis D. Keiser Jr.[a]

[a] *Idaho National Laboratory, Idaho Falls, ID 83415, USA*

* Corresponding author

Email addresses: Jordan.Evans@inl.gov, Mark.DeHart@inl.gov, Kevan.Weaver@inl.gov, Dennis.Keiser@inl.gov

Abstract

Burnable absorbers can benefit nuclear reactors of virtually any design by providing reactivity control for extended fuel cycles, tritium production, burning of long-lived radionuclides, and reactor safety. When selecting the ideal burnable absorber type and its design, one must consider the resulting impact on the reactor's fuel cycle design and cost, reactivity, thermal hydraulics, manufacturing, and radiation response. These selection criteria, as well as neutronic and thermophysical material property requirements, may be vastly different depending on whether the burnable absorber is intended for use in a commercial water-cooled reactor, a research reactor, or a next-generation advanced reactor system. A recent integration, synthesis, description of past and present technologies, and identification of existing gaps and areas of future research is lacking on these important topics. This paper includes a fundamental description of the use of burnable absorbers and their impacts on reactivity, absorber depletion, self-shielding, basic thermophysical properties, and the use of burnable absorbers in next-generation nuclear applications.

Key Words

Burnable absorbers, self-shielding, fabrication, thermomechanical properties

Table of Contents

Nomenclature

γ	Initial self-shielding coefficient
η	BA content
κ	Thermal conductivity
$\sigma_{a,th}$	Absorption cross section for thermal (0.0253 eV) neutrons
$\sigma_{a,BA}(E)$	Energy-dependent neutron absorption cross section of the BA
$\sigma_{a,F}(E)$	Energy-dependent neutron absorption cross section of the fuel
$\sigma_{a,fast}$	Absorption cross section for 200 keV neutrons

$\Sigma_{a,BA}$	The macroscopic absorption cross section of the BA when ignoring self-shielding
$\Sigma_{a,BA,eff}$	The effective macroscopic absorption cross section of the BA when accounting for self-shielding
$\Phi_{BA}(E)$	Energy-dependent neutron flux within the BA
$\Phi_{BA}(0)$	The neutron flux incident upon a BA
$\Phi_{BA}(x)$	The neutron flux after traveling a distance x through a BA
a_i	Coefficients describing the geometry and properties of the medium surrounding the BA
AEC	Atomic Energy Commission
AGR	Advanced gas-cooled reactor
ATF	Accident-tolerant nuclear fuel
ATR	Advanced Test Reactor
b	Barns (10^{-24} cm^{-2})
BA	Burnable absorber
BAR	Burnable absorber rod
BOC	Beginning of cycle
BR	Breeding ratio
BR_{BA}	Burnout rate of the BA
BSG	Borosilicate glass
BWR	Boiling water reactor
CANDU	Canadian deuterium-uranium reactor
CRW	Control rod withdrawal
CVD	Chemical vapor deposition
DOE	United States Department of Energy
E	Energy, neutron energy spectrum, or Young's modulus of elasticity
EOC	End of cycle
ETR	Engineering Test Reactor
eV	Electron volt
f_{BAF}	Neutron absorptions occurring in the BA divided by neutron absorptions occurring in the fuel
FLIP	Fuel Lifetime Improvement Program
g	Self-shielding factor
GA	General Atomics
GAIN	Gateway for Accelerated Innovation in Nuclear
GE	General Electric
GWd/tHM	Gigawatt-day per metric ton of heavy metal
HEU	Highly enriched uranium
HPRR	High Performance Research Reactor (Program)
HTGR	High temperature gas-cooled reactor
HWR	Heavy water reactor
IFBA	Integral fuel burnable absorber
IPyC	Inner pyrolytic carbon
LEU	Low enriched uranium
LOCA	Loss of coolant accident
LOFA	Loss of flow accident
LWR	Light water reactor
M	BA additive
MNSR	Miniature Neutron Source Reactor
MTR	Materials Test Reactor
N_{BA}	Atom density of the BA
N_F	Atom density of the nuclear fuel
NRC	United States Nuclear Regulatory Commission
OPyC	Outer pyrolytic carbon
ORNL	Oak Ridge National Laboratory
P	Porosity
P/A	Peak-to-average fission ratio
PWR	Pressurized water reactor

QUADRISO	Quadruple isotropic
$\vec{r}$	Spatial location
R&D	Research and development
RERTR	Reduced Enrichment for Research and Test Reactors (Program)
S	Lump surface area of the BA
SLOWPOKE	Safe LOW-Power Kritical Experiment
SFR	Sodium-cooled fast reactor
SPS	Spark plasma sintering
t	Time
t_d	BA thickness
t_r	Reduced temperature
T	Temperature
T_f	Integrated flux-time
TD	Theoretical density
TPBAR	Tritium-producing burnable absorber rod
TRIGA	Training, Research, Isotopes, General Atomics (reactor)
TRISO	Tri-structural isotropic
V	Lump volume of the BA, or volume fraction of composite constituent
WABA	Wet annular burnable absorber
WF	Weight fraction
$W(z)$	Lambert W-function
XRD	X-ray diffraction

1. Introduction

Burnable absorbers (BAs), also known as burnable neutron poisons, are materials inserted into a nuclear reactor core that contain non-fissile nuclei with large neutron-absorption cross sections. The BAs absorb neutrons, decreasing their population significantly over the course of the core's operational cycle. As the BA abundance decreases, so too does the BA's impact on reactivity. BAs can provide a variety of benefits, including reactivity control for extended fuel cycles [1-6], tritium production [7], and burning of long-lived radionuclides from spent nuclear fuel [8, 9]. While BAs can vary widely based on economics, thermal hydraulics, manufacturing, response to radiation damage, and reprocessing/disposal, BAs have a strong negative reactivity worth, which of course decreases by design as they are depleted due to neutron absorption. This paper provides the integration, synthesis, and description of past and present burnable absorber technologies. Furthermore, it seeks to identify existing gaps and areas of future research with respect to burnable absorbers which is currently lacking in the recent peer reviewed literature. An example is also provided which illustrates the impact of burnable absorbers on neutron multiplication and fission (power) densities based on Monte Carlo neutronic simulations of the Advanced Test Reactor (ATR).

Burnable absorbers are often used to reduce power peaking in the core, either for a fresh fuel assembly (typically in light water reactors (LWRs)) or locally within a fuel pin or plate (typically in research and test reactors). The negative reactivity of a BA offsets the positive reactivity of fresh fuel. Depletion of fuel is accompanied by depletion (burnout) of the BA material; ideally, the BA will effectively burn out at the same rate as the fuel in such a way that the net reactivity remains constant with time. If the BA burns out too quickly, then a positive reactivity swing later in the operational fuel cycle could exceed the allowable limits for the reactor. If the BA burns out too

slowly, then the remaining BA results in a negative reactivity penalty toward the end of the fuel's operational cycle; however, an exact match is not necessary and typically is not feasible. Local spectral effects will affect the relative depletion of the poison and the fuel. When used in this manner, BA materials may be included within the fuel, either as a homogeneous mixture or a coating, but BA rods can also be used to control local power peaking for a fuel assembly by appropriate placement of rods within a fuel assembly. The two approaches are often combined; gadolinium-bearing fuel rods are used to control assembly reactivity in many boiling water reactor (BWR) designs (*vide infra*). Pressurized water reactors (PWRs) also use soluble boron to control total core reactivity, but because the boron is uniformly distributed in the coolant it is not used to control peaking. Further, soluble boron is not considered to be a burnable absorber as reactivity control is managed by reactor operators by reducing boron content with burnup over a fuel cycle.

Because neutron capture in burnable absorbers is typically spectrum-dependent, BAs are sensitive to changes in temperature. ^{10}B, often used as a burnable poison, is a 1/v absorber whereby its neutron absorption cross section decreases logarithmically with neutron energy. The magnitude of negative reactivity for ^{10}B decreases with increasing temperature as the thermal Maxwellian shifts toward higher energies. This results in net positive reactivity feedback. ^{155}Gd and ^{157}Gd, on the other hand, while 1/v at very low neutron energies, both have significant resonances above 1 eV and can a exhibit increasingly negative reactivity coefficient with respect to temperature, depending on the spectrum of the reactor itself. ^{167}Er has a large thermal resonance at 1 eV that results in increased absorption resulting in a negative reactivity coefficient with respect to temperature; hence, boron and gadolinium are also common BA materials in fast reactors; in a fast reactor spectrum both have removal cross sections that decrease with increasing temperature, so both have net positive temperature reactivity coefficients. While a negative reactivity coefficient for a BA would be desirable in a reactor such that neutron capture increases with increasing temperature, the temperature reactivity coefficient of fuel associated with burnable absorbers is designed to always be negative and will more than offset any positive feedback from burnable absorbers. Of course, the magnitude of the temperature reactivity coefficient will always decrease with burnout of the poison materials.

BAs are considered distinctly separate from control rods. Control rods in nuclear reactors can be withdrawn from the reactor core during operation and can be used for several years to decades before replacement is necessary. Other neutron poisons that are present in the core that are released as fission products are also not considered BAs; instead, they are an unavoidable consequence of nuclear fission reactions.

Different nuclear reactor types have different operating conditions, coolants, fuel forms, and neutron spectra which may limit the practicality of some BAs. The discussion offered in this paper will focus on the most common BAs listed in **Table 1**, where $\sigma_{a,th}$ and $\sigma_{a,fast}$ are the neutron absorption cross sections at thermal (0.025 electron-volts (eV)) and fast (200 keV, which is the flux peak for a typical sodium-cooled fast reactor) neutron energies, respectively, in units of barns (10^{-24} cm^2). Cross-section data for this paper were taken from the ENDF/B-VII.1 library [10]. Some isotopes have been omitted from **Table 1** because they are either highly unstable, have no natural abundance (i.e., are synthetic), or do not readily absorb neutrons.

As noted earlier, the most common BA materials in commercial LWRs are boron and gadolinium. Boron is used in the standard form of B_4C with the natural boron isotopic composition (approximately 19.9% ^{10}B and 80.1% ^{11}B). ^{10}B has a thermal neutron cross-section of about 3850 b; in comparison, thermal absorption in ^{11}B is negligible, with a cross section of about 0.005 b for thermal neutrons. When absorbing a thermal neutron, ^{10}B emits an alpha particle (^4He) resulting in a ^7Li daughter nucleus. As both are stable isotopes, neither is a source of decay heat post-shutdown. However, the accumulation of helium can produce internal pressure that can challenge the integrity of high-density fuels or build up between the poison and cladding. Further, neutron capture in ^7Li results in the production of tritium. Natural gadolinium (see **Table 1** for isotopic abundances and cross sections) is another common BA in commercial reactors due to the high neutron absorption cross section of ^{155}Gd and ^{157}Gd. Their absorption cross-sections are the highest among all stable isotopes. Relative to boron and other BA materials, which are generally considered to be "gray" absorbers, gadolinium behaves like a "black" absorber for neutrons, making it highly effective in compensating for excess reactivity. However, this same property can result in strong local flux depressions if not properly designed [11]. This phenomenon will be discussed in detail in the next section.

Although not as common, hafnium-based materials are attractive BA candidates, not only because of their ability to readily absorb neutrons above thermal energies (a phenomenon known as resonance energy absorption), but also because its worth changes slowly with irradiation. This slow change is due to the multi-isotope capacity for Hf to absorb neutrons. In Hf, when a neutron is absorbed, some natural hafnium isotopes readily transform into another neutron-absorbing isotope. Hafnium metal also has excellent corrosion resistance to hot water if a passivation layer (HfO_2) forms on its surface. In its unalloyed form, passivated hafnium corrodes in 400 °C steam at a rate of approximately 1.36 $\mu g \cdot cm^{-2} \cdot day^{-1}$, about $1/8^{th}$ the rate of Zircaloy-2 [12]. Without this passivation layer, however, hafnium degrades rapidly due to the diffusion of hydrogen formed by radiolysis of water, resulting in rapid swelling and embrittlement [13]. This hydride-induced swelling and facture of hafnium has led to the abandonment of hafnium as an absorber material under high temperature/fluence conditions (i.e., commercial applications).

Hafnium-based BAs can also designed HfO_2. In principle, HfO_2 could be used as a BA material. While UO_2 adopts a fluorite crystal structure, HfO_2 can crystallize in monoclinic, tetragonal, or cubic structures. For high temperature conditions, for example in commercial UO_2, where the centerline fuel temperature can exceed 1300 K, HfO_2 may substitute uranium to form the UO_2-HfO_2 solid solution [14]. Nuclear fuel might also be coated with a layer of HfO_2 via a deposition technique, though there is no evidence of this being experimentally tested under reactor conditions [15-18].

Cadmium-based BAs have attractive neutronic properties for extended fuel cycles. Cadmium is also an important component of standard silver-indium-cadmium control rods in both research and commercial nuclear reactors. The neutronic properties of Cd-based BAs allow precise control of BA burnout over a wide range of fuel burnup in comparison to boron (slower-burning) or gadolinium (faster-burning) BAs [19, 20]. Further, cadmium's (n,γ) reaction does not result in helium accumulation. Historically, proposed cadmium-based BAs have taken the form of metallic

Cd wires or CdO pellet coatings [21-24]. The use of Cd-based BAs, however, presents fabrication and disposal complications due to significant health concerns. Both Cd and CdO are ranked as a health hazard Level 4 according to the National Fire Protection Association. Very short exposure to small amounts of either of these materials can be lethal, as they are carcinogenic, can cause lung oedema and death if inhaled, and are extremely toxic if ingested. Further, the 350°C melting point of cadmium metal limits its applicability, particularly during a possible design-basis accident.

Table 1: Selected nuclei properties and neutron absorption cross sections.

Element	Isotope	Half-Life	Natural Isotopic Abundance (%)	Reaction	$\sigma_{a,th}$ (b)	$\sigma_{a,fast}$ (b) [(1)]
Li	^{6}Li	Stable	7.5	n,α	938	1.97
B	^{10}B	Stable	19.9	n,α [(2)]	3844	1.47
Ag	^{107}Ag	Stable	51.8	n,γ	38	0.31
	^{109}Ag	Stable	48.2	n,γ	90	0.29
Cd	^{113}Cd	$8\cdot10^{15}$ y	12.2	n,γ	19969	0.28
In	^{113}In	Stable	4.3	n,γ	12	0.35
	^{115}In	$4\cdot10^{14}$ y	95.7	n,γ	202	0.29
Sm	^{147}Sm	10^{11} y	15.0	n,γ	57	0.32
	^{149}Sm	Stable	13.8	n,γ	40150	0.70
	^{150}Sm	Stable	7.4	n,γ	100	0.25
	^{152}Sm	Stable	26.7	n,γ	206	0.15
Eu	^{151}Eu	$5\cdot10^{18}$ y	47.8	n,γ	9185	0.30
	^{153}Eu	Stable	52.2	n,γ	358	0.75
Gd	^{154}Gd	Stable	2.18	n,γ	85	0.37
	^{155}Gd	Stable	14.8	n,γ	60737	0.73
	^{156}Gd	Stable	20.5	n,γ	2	0.19
	^{157}Gd	Stable	15.7	n,γ	252912	0.33
	^{158}Gd	Stable	24.8	n,γ	2	0.08
	^{160}Gd	Stable	21.9	n,γ	1.4	0.04
Dy	^{161}Dy	Stable	18.9	n,γ	600	0.45
	^{162}Dy	Stable	25.5	n,γ	194	0.13
	^{163}Dy	Stable	24.9	n,γ	123	0.34
	^{164}Dy	Stable	28.3	n,γ	2653	0.05
Er	^{167}Er	Stable	22.9	n,γ	650	0.51
Lu	^{175}Lu	Stable	97.4	n,γ	23	0.49
	^{176}Lu	$4\cdot10^{10}$ y	2.6	n,γ	2098	0.72
Hf	^{174}Hf	$2\cdot10^{15}$ y	0.16	n,γ	550	0.45
	^{177}Hf	Stable	18.6	n,γ	374	0.56
	^{178}Hf	Stable	27.3	n,γ	84	0.10
Ir	^{191}Ir	Stable	37.3	n,γ	954	0.44
	^{193}Ir	Stable	62.7	n,γ	111	0.36

(1) $\sigma_{a,fast}$ is defined here as the neutron absorption cross section at 200 keV—i.e., the energy of the flux peak for a typical sodium-cooled fast reactor.

(2) The n,2α cross section for ^{10}B increases by several orders of magnitude above 1 MeV and exceeds that of the n,α cross section above 4.7 MeV. This makes boron-based BAs particularly attractive for fast reactor applications from a neutronics perspective.

2. Absorber Burnout and Heterogenous Effects

The time-dependent behavior of BAs used for reactivity control is dependent on several factors, including the local flux and self-shielding effects. The latter can be classified in terms of spatial or energy self-shielding. The degree of self-shielding also defines whether a design can be homogenous (minimal self-shielding) or heterogeneous in terms of BA design and placement. Each has its benefits and disadvantages for a given core design. These topics are reviewed in this section.

2.1 Absorber Burnout

One of the most important criteria that drives the BA selection is its burnout rate due to neutron capture. Some elements, such as boron, have only one stable isotope that readily absorbs neutrons (^{10}B) while other elements have multiple neutron-absorbing isotopes, resulting in subsequent neutron absorptions. For the simplest case of BAs with only one neutron-absorbing isotope and infinitely dilute, i.e., no self-shielding (*vide infra*), the burnout rate can be calculated using **Equation 1** [25]. Once such a BA nuclide absorbs a neutron, it is changed to the next higher mass isotope, which may be stable or decay; in either case, the daughter product is not an absorber. Such a BA can be depleted rapidly if its absorption cross section is large. Note that the cross section and flux both depend on the neutron energy spectrum, meaning that nuclei which have high thermal neutron absorption cross sections may not be effective BAs for fast spectrum nuclear reactors, or vice versa.

$$BR_{BA} = N_{BA} \cdot \sigma_{a,BA}\left(E\right) \cdot \Phi_{BA}\left(E\right) \qquad \textbf{(Eq. 1)}$$

where

BR_{BA} = burnout rate of the BA (atoms·s^{-1}·cm^{-3})
N_{BA} = atom density of the BA (atoms·cm^{-3})
$\sigma_{a,BA}(E)$ = energy-dependent neutron absorption cross section of the BA (cm^2 = 10^{-24} b)
$\Phi_{BA}(E)$ = energy-dependent neutron flux within the BA (neutrons·s^{-1}·cm^{-2})
E = neutron energy spectrum

Some elements have multiple naturally occurring isotopes which readily absorb neutrons. For example, europium has two stable isotopes (^{151}Eu and ^{153}Eu) as shown below, along with each isotope's natural abundance and thermal neutron absorption cross sections (some isotopes with small absorption cross sections are ignored). For the case of a europium-based BA, the burnout rates of the relevant Eu isotopes are described by a set of coupled differential equations in **Equation 2** that relate production (absorption by the next lower isotope) and loss (absorption and decay) [26]. These coupled equations, known as the Bateman equations, can be solved numerically

or analytically to determine the isotopic populations and burnout rates as a function of time [26]. Here, it is assumed that the europium is distinct from the fuel and is not produced as a function of fission. The full set of Bateman equations also must consider the fact that a daughter product from either transmutation or decay may also have a significant absorption cross section, and in principle, all transmutation mechanisms should be included in **Equation 2**. For simplicity, however, only decay and radiative capture (absorption) of Eu isotopes are shown here; nevertheless, we still obtain seven coupled equations for isotopes.

Abundance (%)	47.8		0		52.2		0		0		0		0
Isotope	^{151}Eu	→	^{152}Eu	→	^{153}Eu	→	^{154}Eu	→	^{155}Eu	→	^{156}Eu	→	^{157}Eu
$\sigma_{(n,\gamma),th}$ (b)	9185		12796		358		1353		3760		100		111

$$\frac{d^{151}N}{dt} = -^{151}N(t)\cdot^{151}\sigma_a(E)\cdot\Phi(E) - ^{151}N(t)\cdot^{151}\lambda \qquad \textbf{(Eq. 2)}$$

$$\frac{d^{X}N}{dt} = ^{(X-1)}N(t)\cdot\left(^{(X-1)}\sigma_{n,\gamma}(E)\cdot\Phi(E) - ^{(X-1)}\lambda\right) - ^{X}N(t)\cdot\left(^{X}\sigma_a(E)\cdot\Phi(E) - ^{X}\lambda\right)$$

where,

λ = Radioactive decay constant (s^{-1})

X = [152, 157]

If breeding (the conversion of fertile nuclei into fissile nuclei) and fission are ignored, then the relationship for the burnout rate of the fuel in the reactor, BR_F, is identical to that of the burnable absorber in **Equation 1**, where N_F, $\sigma_{a,F(E)}$, and $\Phi_F(\bar{r},E)$ are the fuel's atom density, neutron absorption cross section, and neutron flux within the fuel, respectively, where $\bar{r}$ represents spatial location.

2.2 Spatial Self-Shielding

Another relevant concept for BA design and reactor operation is the set of phenomena known as self-shielding. In this section, we will discuss spatial self-shielding. In heterogenous thermal reactor cores, neutrons are born by fission within the fuel, but they are moderated, or slowed down, after leaving the fuel and entering the moderator. Lower energy neutrons are scattered back into the fuel to be captured or absorbed to cause another fission to maintain criticality; however, such neutrons can also be scattered into a BA material. BAs are therefore used to compensate for excess reactivity in the fuel to be able to maintain criticality. Because the cross section of a BA is very large relative to fuel fission cross sections at thermal energies, there is a high probability of absorption as soon as the neutron enters the BA region. As a result, the surface layers of the BA

geometrically shield the inner layers from neutron flux, leading to a relatively lower neutron flux inside the absorbing material. For fast reactors, self-shielding is generally negligible – the mean free path of fast neutrons within a fast reactor will be significantly longer that the thickness of an absorber material, so the probability of absorption is approximately constant in moving through a BA material.

The self-shielding factor, *g*, is the ratio of the flux within a burnable absorber region to that which would be observed if the absorber was not present, as defined by **Equation 3** [27]. Here we have assumed that the flux in the absence of the BA is approximately constant in space. In general, there is a significant spatial reduction in the flux within a strong absorber due to neutron absorption. A strong absorber will locally depress the flux within the absorber relative to the flux that would be present in that region in its absence. This is illustrated in a simplified fashion in **Figure 1**. Here, the blue shading represents the poison region in space. The blue line shows the spatial flux in absence of the poison, while the grey line within this region shows the attenuation of the flux in both directions moving through the region, with a minimum in the center of the region (for a symmetric geometry). This complicates the solution of **Equation 2**, as $\Phi(E)$ is not a simple function of energy but inherits a spatial component as well, i.e., $\Phi(\bar{r},E) = g(\bar{r},E)\cdot\Phi_{nBA}(E)$.

$$g(\bar{r},E) = \frac{\Phi_{BA}(\bar{r},E)}{\Phi_{nBA}(E)} \qquad \textbf{(Eq. 3)}$$

where

$\Phi_{BA}(\bar{r},E)$ = energy- and spatially dependent neutron flux within the burnable absorber (neutrons$\cdot s^{-1}\cdot cm^{-2}$)

$\Phi_{nBA}(E)$ = energy-dependent neutron flux within the same region if no burnable absorber is present, i.e. without spatial self-shielding (neutrons$\cdot s^{-1}\cdot cm^{-2}$)

More generally, **Equation 3** can be written in terms of both energy and spatial averages of the fluxes in the absorber region, where the fluxes are volume- and lethargy-weighted averages of space and energy, respectively, as shown in **Equation 4** [27]. However, it is important to note that as the net reactivity of the BA decreases with burnup, the flux in the BA region will increase, trending toward the value of Φ_{nBA}, i.e., similarly *g* will increase and approach unity.

$$g = \frac{\Phi_{BA}}{\Phi_{nBA}} \qquad \textbf{(Eq. 4)}$$

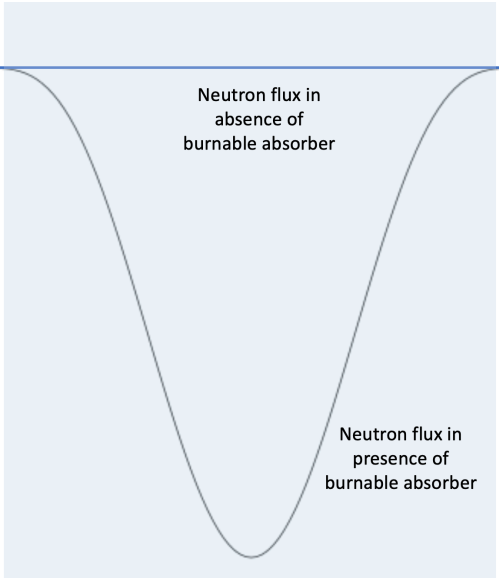

Fig. 1: Illustration of the spatial effect of a strong absorber depressing the neutron flux.

The previous discussion and the plot in **Figure 1** both assume that the BA is composed of a uniform distribution of absorber material. If a BA material is lumped (i.e., non-uniformly distributed as dispersoids, precipitates, thick rings, etc.) with sufficiently large volume, then the distribution of the neutron flux will not be a simple continuous function throughout the BA volume due to spatial variations in self-shielding; however, a volume-averaged distribution is typically assumed in reactor calculations, and has been found to be generally acceptable when dispersoids are randomly located and have an average aspect ratio near unity. On the other hand, some fabrication processes may create distributions in which the absorbing materials are concentrated in limited spatial locations (e.g., located preferentially near the radial center or toward the outside of a rod), or with a very large aspect ratio where the poison material is stretched preferentially in a specific direction (e.g., elongated and aligned in a particular direction due to rolling, extrusion, etc.). In such cases, self-shielding effects may be more pronounced in one direction over another, or strongly vary with location. Thus, such situations demand an understanding of the effect of the distribution and shape of the poison material within the BA to understand the evolution of poison burnout rate and impact on reactivity versus time. It is possible that tailored fabrication methods could be used to achieve desired poisoning behavior. However, developing an understanding of the reactivity worth of non-uniform distributions or use in special applications is beyond the scope of this paper. Henceforth, this discussion will focus on BAs with a poison distribution that can be considered uniform through the media.

The reduction in the neutron flux moving through a fresh burnable absorber material is a result of capture of neutrons which occurs more often at the surface of the rod due to spatial self-shielding. Some neutrons will penetrate or even thermalize within the interior of a BA, but neutrons will be preferentially absorbed at the outer rim. With increasing burnup, the poison nuclide(s) in

the most strongly absorbing region will be converted by neutron capture and possibly also decay to a nuclide or nuclides with a much smaller absorption cross section through one or more successive captures. As poison is transmuted at the outer region of the BA, more neutrons can penetrate further into the absorbing material. Hence, the poison will progressively burn out moving from the outside to the innermost volume in an onion-skin fashion.

Although the discussion above was generalized, it primarily applies to non-fueled BA media. Burnable absorbers may also be combined with fuel rods. Gadolinia (Gd_2O_3) is often used as an integral poison within both PWR and BWR fuel, where it is to a first approximation uniformly blended with UO_2 (*vide infra*). In such fuel, self-shielding is also present due to a large thermal cross section for fission in ^{235}U. The same radial burnup effect exists in gadolinia-bearing fuel. By design, the gadolinium burns out well in advance of the fuel; its purpose is intended to offset the initial high reactivity of fuel enrichments in the 4-5 wt% ^{235}U enrichment range of commercial power reactors. Westinghouse's Integral Fuel Burnable Absorber (IFBA) [28, 29] also adds poison material to a fuel rod, although in this case, fuel pellets are coated with a thin layer of zirconium diboride (ZrB_2). Again, although some thermal neutrons will pass through the coating while a significant number of them will be captured by the ^{10}B in the ZrB_2 coating. This reduces the burnup of the fuel such that by the time the boron is depleted the IFBA fuel (and the core as a whole) will have lost the excess reactivity it had at the beginning of the fuel cycle due to a combination of fuel depletion and fission product buildup.

2.3 Energy Self-Shielding

A phenomenon known as energy self-shielding is also present in fuel rods. Specific resonance energies in ^{235}U have large cross sections relative to adjacent energy regions. Hence, neutrons at those energies are highly likely to be captured, reducing the thermal flux in energies close to the resonance. Here, flux is reduced on the energy spectrum, not on the spatial spectrum, although this does result in some spatial self-shielding at those resonance energies. For BAs, however, cross sections have a spectral variation, but low energy resonances are rare. ^{155}Gd and ^{157}Gd, the two strongly absorbing gadolinium isotopes, have some resonances near 1 eV, but below 1 eV there are no resonances and the cross section becomes one to two orders of magnitude larger in the thermal region. Boron has no resonances below 1 MeV, and the thermal cross section is four to five times larger in the thermal region than that of the higher energy resonances. Hence, energy self-shielding is not normally considered with respect to common BA materials.

Finally, it is important to observe that BAs may be permanent within a reactor fuel assembly, residing in the assembly for its entire lifetime– this is always true when the poison is integral to the fuel. However, most LWRs are designed to be able to remove BA-bearing structures, typically after the first cycle. In PWR designs, a cluster of burnable poison rods may be loaded in control rod positions for uncontrolled assemblies. In BWRs, temporary poison curtains (plate-type structures) are used between uncontrolled fuel assemblies. For both concepts, the BA loading is such that it is fully burned out by the end of the first cycle. During fuel shuffling operations the depleted poison structures are removed. This approach may be applied in fuel block shuffling for gas-cooled reactor designs, and BA materials may be used within pebble bed reactors during their

approach to their asymptotic fuel distribution. For evolving contemporary microreactor concepts, however, where fuel shuffling is not anticipated, BA rods or plates may be desirable with a significant loading to offset high loadings of fuel and may be designed to last on the order of the designed core life. However, whether removed or not, the self-shielding factor *g* due to the poison will approach unity near the end of the effective life of the BA. This means that the boron absorption effect is gone, and thermal neutrons will pass freely (perhaps with scattering but very little absorption) through the depleted BA region.

2.4 Heterogeneity vs. Homogeneity in BA Distribution

There is no clear distinction between when it is appropriate to assume homogeneous vs. heterogeneous BA geometry; for the case of ^{10}B-containing compounds (whose 0.0253 eV neutron absorption cross section is about 3838 b), thermal neutron self-shielding effects are noticeable when the BA's physical thickness reaches length scales on the order of a few microns [30]. In the analytical treatment for the burnout of a self-shielded BA lump, any approximation to the one-velocity Boltzmann equation may be represented by a power series in the quantity of absorber located in the lump as shown in **Equation 5** [27].

$$g = \left[1 + \sum_{i=1}^{\infty} a_i \left(2 t_d \Sigma_{a,BA} \right)^i \right]^{-1} \qquad \textbf{(Eq. 5)}$$

$$\Sigma_{a,BA,eff} = g \Sigma_{a,BA}$$

where

a_i = Coefficients describing the geometry and properties of the medium surrounding the BA

t_d = BA thickness

$\Sigma_{a,BA} = \sigma_{a,BA}(E) \cdot N_{BA}$ = the macroscopic absorption cross section of the BA when ignoring self-shielding

$\Sigma_{a,BA,eff}$ = the effective macroscopic absorption cross section of the BA when accounting for self-shielding

In most practical situations, the a_i decrease rapidly after the first term. Using only the first term in the expansion offers a reasonable approximation for illustrative purposes such that the self-shielding factor is given by **Equation 6** [27].

$$g = \left[1 + \frac{\gamma N_{BA}(t)}{N_{BA}(0)}\right]^{-1} \quad \textbf{(Eq. 6)}$$

where

t = duration that the BA has been under neutron irradiation (sec)

$N_{BA}(t)$ = atom density of the BA at time t (atoms·cm^{-3})

$N_{BA}(0)$ = atom density of the fresh BA, i.e., at time $t = 0$ (atoms·cm^{-3})

γ = initial self-shielding coefficient, defined by the initial lump geometry and initial macroscopic absorption cross section

Since γ is a constant, the assumptions made thus far allow direct calculation of the burnout rates for the fuel and BA. Still exclusively considering thermal neutrons for this calculation, the fuel burnout rate is defined by **Equation 7** and the BA burnout rate is defined by **Equation 8** [30]. The burnout rate ratio is determined by combining **Equations 7** and **8** as shown in **Equation 9** [30].

$$dx = -\sigma_{a,F} n v_0 x dt \quad \textbf{(Eq. 7)}$$

$$dy = -\sigma_{a,BA} n v_0 \frac{y dt}{1 + \gamma y} \quad \textbf{(Eq. 8)}$$

$$\frac{dx}{dy} = \frac{\sigma_{a,F}}{\sigma_{a,BA}} \frac{x(1 + \gamma y)}{y} \quad \textbf{(Eq. 9)}$$

where

$$x(t) = \frac{N_F(t)}{N_F(0)}$$

$$y(t) = \frac{N_{BA}(t)}{N_{BA}(0)}$$

nv_0 = thermal neutron flux at $t = 0$

Using the initial conditions that *x(0) = y(0) = 1* yields the burnout rate relationship between the fuel and the BA as shown in **Equation 10** [30]. Note that an initial self-shielding coefficient of $\gamma = 0$ indicates that there are no BA self-shielding effects (e.g., if it is distributed homogeneously in a diffuse manner), reducing to **Equation 11** [30].

$$x = \left[y e^{\gamma(y-1)} \right]^{\left(\frac{\sigma_{a,F}}{\sigma_{a,BA}} \right)} \quad \textbf{(Eq. 10)}$$

$$x = y^{\left(\frac{\sigma_{a,F}}{\sigma_{a,BA}} \right)} \quad \textbf{(Eq. 11)}$$

where

$\gamma = 0$ (i.e., no self-shielding)

It may be more practical to define reactor operation time in terms of integrated flux-time T_f using **Equation 12** [27]. Consequently, we can see by inspection with **Equation 2** and **Equation 5** that the rate of change in the BA population is given by **Equation 13** as a function of flux-time [27]. Integrating **Equation 13** yields the relationship of the burnable poison population at flux-time T_f in **Equation 14** [27].

$$T_f = \int \Phi dt \quad \textbf{(Eq. 12)}$$

$$\frac{dN_{BA}(T_f)}{dT_f} = -N_{BA}(T_f) \cdot \sigma_{a,BA} \cdot g = \frac{-N_{BA}(T_f) \cdot \sigma_{a,BA}}{1 + \frac{\gamma N_{BA}(T_f)}{N_{BA}(0)}} \quad \textbf{(Eq. 13)}$$

$$T_f = \frac{\gamma}{\sigma_{BA}} \left[1 - \frac{N_{BA}\left(T_f\right)}{N_{BA}\left(0\right)} - \frac{1}{\gamma} \ln\left(\frac{N_{BA}\left(T_f\right)}{N_{BA}\left(0\right)} \right) \right] \quad \textbf{(Eq. 14)}$$

Rearranging and solving **Equation 14** for the BA population as a function of integrated flux-time yields **Equation 15** where *W(z)* is the Lambert W-function. Several mathematical computing software packages implement the Lambert W-function (e.g, Maple, Matlab, Mathematica). For the

case where the BA has no self-shielding, $\gamma = 0$ and the BA population vs. flux-time can be determined directly using **Equation 16**.

$$\frac{N_{BA}\left(T_f\right)}{N_{BA}\left(0\right)} = \frac{W\left(\gamma e^{\gamma - \sigma_{a,AB} \cdot T_f}\right)}{\gamma} \qquad \textbf{(Eq. 15)}$$

where

$\gamma > 0$ (i.e., accounts for BA self-shielding)
$W(z)$ = the Lambert W-function

$$\frac{N_{BA}\left(T\right)}{N_{BA}\left(0\right)} = e^{-\sigma_{a,AB} \cdot T_f} \qquad \textbf{(Eq. 16)}$$

where

$\gamma = 0$

Equation 15 and **Equation 16** only consider monoenergetic neutron absorption. The absorption cross sections of most BA isotopes vary strongly with energy, as shown in **Figure 2** for the case of ^{10}B [31]. If we assume that the average neutron energy in a reactor is 0.0253 eV, indicated by the solid red circle in **Figure 2**, this correlates to a ^{10}B neutron absorption cross section of about 3838 b. The flux peak for a typical fast reactor, about 200 keV, is indicated by the dashed green triangle in **Figure 2,** which correlates to a neutron absorption cross section of about 1.5 b [10]. Using the 0.0253 eV cross section in the one-group approximation, the BA population vs. integrated flux-time can be compared for different levels of the BA initial self-shielding coefficient, γ, as shown in **Figure 3** below. Note that increasing the initial self-shielding coefficient decreases the rate at which the BA depletes, thereby increasing its lifetime in the core.

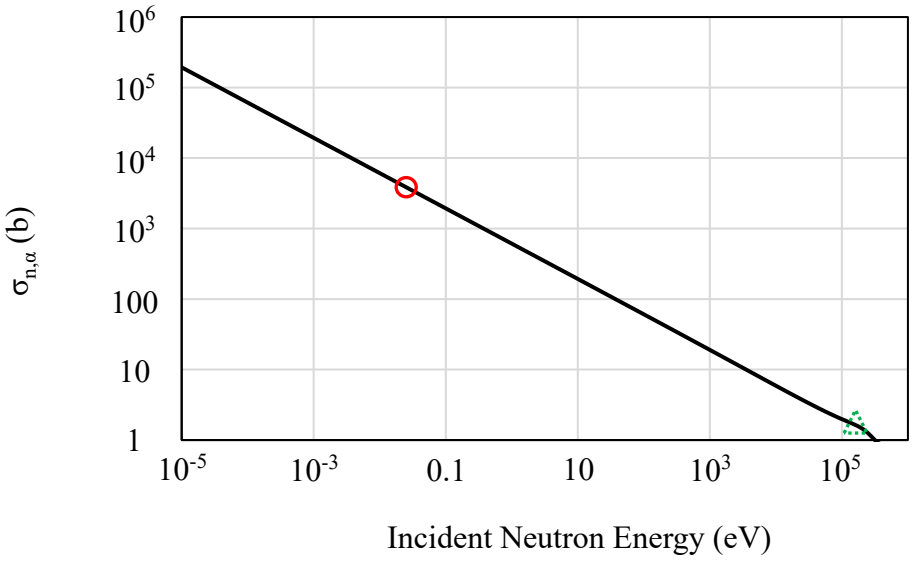

Fig. 2: $\sigma_{n,\alpha}$ vs. energy for ^{10}B. The solid red circle corresponds to 0.0253 eV, for which $\sigma_{n,\alpha}$ = 3838 b. The dashed green triangle corresponds to 200 keV (a typical fast reactor flux peak), for which $\sigma_{n,\alpha}$ = 1.5 b.

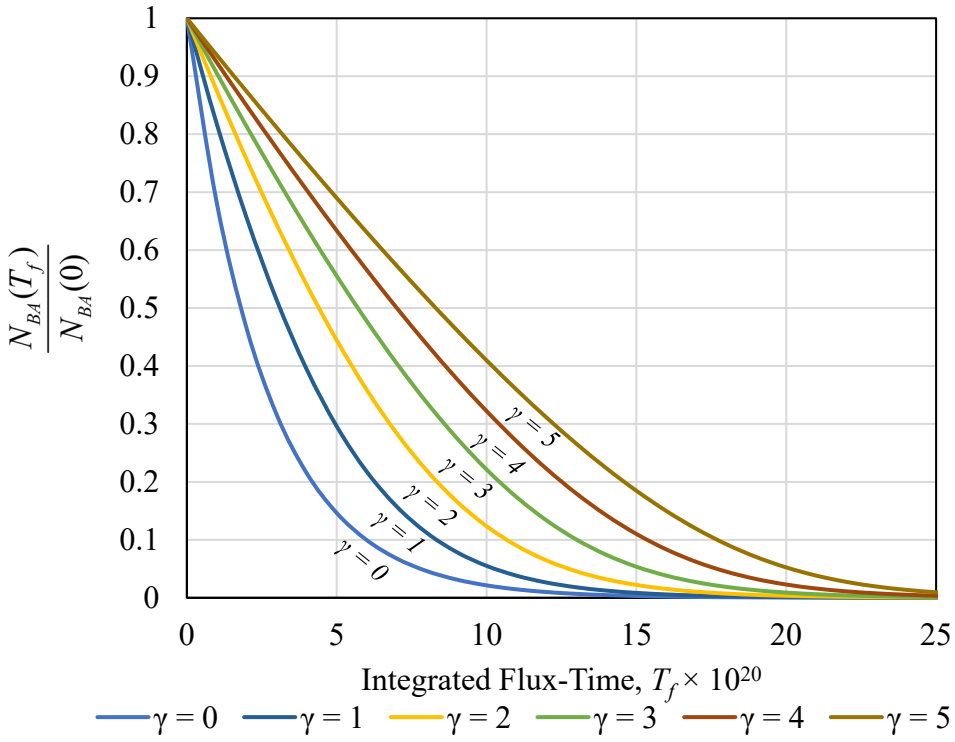

Fig. 3: Comparison of self-shielded ($\gamma > 0$) and non-self-shielded ($\gamma = 0$) burnable absorber concentrations vs. integrated flux-time, from **Equation 15** and **Equation 16**.

3. Burnable Absorbers for Commercial Water-Cooled Reactors

Commercial water-cooled reactors generally have three distinct designs: pressurized water reactors (PWRs), boiling water reactors (BWRs), and heavy water reactors (HWRs). At the beginning of cycle (BOC) for a commercial nuclear reactor's operational fuel cycle, the core has excess reactivity because (a) the fissile content of a fuel assembly is maximal at BOC and (b) accumulation of fission product neutron poisons has not yet begun in fresh fuel. Control rods can be used to counteract the excess reactivity at BOC; however, inserting control rods deeper into the reactor core causes the power distribution to become increasingly nonuniform. Using control rods for this purpose also decreases the effective control rod lifetime. In commercial PWRs, soluble neutron absorbers (typically boric acid) are routinely introduced into the primary coolant to provide uniform negative reactivity. The utility of soluble neutron absorbers, however, is limited in water-moderated reactors because at higher concentrations they also diminish the moderator void coefficient of reactivity, which must remain negative throughout the operational fuel cycle.

Ideally, the BA (and its neutron-absorbing daughter products) should be depleted shortly before the reactor's end of cycle (EOC). In current LWRs, incorporating boron, gadolinium, or erbium compounds into the fuel rods or non-fueled rodlets is common. Commercial HWRs, such as Canadian deuterium-uranium (CANDU) reactors, often incorporate dysprosium BAs into the non-plutonium-bearing depleted uranium fuel rods.

When selecting and designing a BA for use in commercial nuclear reactors in the United States, the BA's impact on safety and behavior of the spent fuel at discharge must be rigorously established to obtain regulatory approval through the Nuclear Regulatory Commission (NRC). Selection, design, and certification of BAs will always depend upon detailed analyses of the BA impact on reactivity. The neutronics optimization of BAs in commercial water-cooled nuclear reactors has been studied extensively, but the conclusions of such studies often vary depending on the particular design and conditions of the system in which the BA will be used [32-34]. However, it is important to remember that the primary reasons to use BAs in commercial nuclear power reactors are to reduce fuel cycle costs, extend the fuel's operational cycle, and improve reactor safety. BA designs have been proposed, based purely on neutronic rationale, which attempt to maximize BOC vs. EOC reactivity effects by using transuranics, like ^{240}Pu [8] or $^{241\text{-}243}$Am [9, 35, 36], as the BA species. While it is true that such transuranic BAs will add to EOC reactivity by transmuting into fissile species, economic, licensing, manufacturing, handling, and proliferation implications must also be considered. As a result, the following aspects of BAs in commercial water-cooled reactors will be discussed: an introduction to the two general types of BAs currently used (fueled vs. non-fueled burnable absorbers), fabrication, and material properties.

3.1 Fueled Burnable Absorbers

One current method of including BAs into commercial nuclear reactor cores is to incorporate the BA material within or around the UO_2 fuel pellets themselves. Three common fueled BA

designs are illustrated in **Figure 4**, where the BA is (left) dispersed or homogeneously mixed within the UO_2 matrix, (middle) coating the outer surface of the UO_2 pellet, or (right) both. Design of boron-based BAs must account for the production and accumulation of helium from the $^{10}B(n,\alpha)^{7}Li$ reaction, which could reduce fuel thermal conductivity, increase fuel temperature, and accelerate fission gas release if the reaction occurs from within the fuel matrix itself [37]. Consequently, boron is only incorporated into commercial LWR fuel in the form of external coatings. In practice, commercial water-cooled reactors use fuel-BA pellets of UO_2-Gd_2O_3, UO_2-Er_2O_3, or UO_2-Dy_2O_3 dispersions or solid solutions mixed within the fuel. Westinghouse Electric Company also produces standard UO_2 fuel coated with a thin ZrB_2 film, called an integral fuel burnable absorber (IFBA) [28, 29]. The ideal BA isotopics, design, and distribution depend not only on the type of reactor, but also on the details of the fuel pin assembly design itself [38].

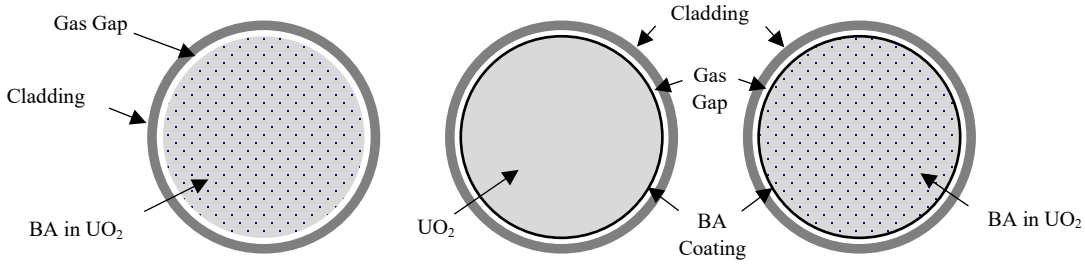

Fig. 4: Three common fuel-BA designs for commercial reactors, where the BA is (left) dispersed or homogeneously mixed within the UO_2 matrix, (middle) coating the outer surface of the UO_2 pellet, or (right) both.

3.2. Burnable Absorber Rods

Another common BA design for commercial water-cooled reactors is burnable absorber rods (BAR, typically called "burnable poison rods" in industry). BARs are loaded in guide tube positions in an assembly and are typically removed when the fuel is shuffled; hence it is desirable to have the poison worth reduced to as small as possible by the end of the fuel's operational cycle. Two examples of such BARs are the Westinghouse wet annular burnable absorber (WABA) rodlets and (the less common) borosilicate glass (BSG) burnable absorber. WABAs and BSGs contain no fissile material. Because the BA and fuel are not mixed, helium buildup due to n,α reactions does not impact the fuel's thermal conductivity, internal fuel gas pressure, nor fission gas release.

The WABA is an annular BA that is clad in two concentric Zircaloy tubes, while the BSG is clad in concentric 304 stainless steel tubes. An illustration of typical WABA and BSG BAs are shown in **Figure 5**. Each rodlet requires an annular plenum to accommodate the release and buildup of helium during use, as well as contact with water for cooling purposes. The water flowing through the innermost channel also augments thermalization of neutrons, reducing the necessary BA thickness and allowing more controllable and complete burnout of BA material [33]. Similar

concepts have been proposed whereby BAs are incorporated into other in-core components, such as thimble guides [39, 40]. The compositions of WABA and BSG BAs are provided in **Table 2** [41].

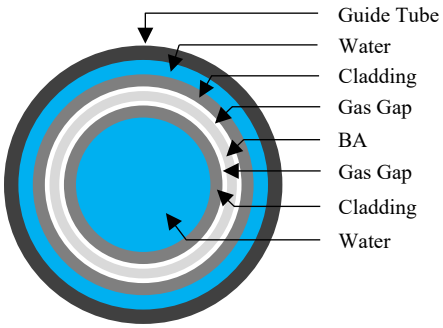

Fig. 5: Illustration of WABA or BSG used in commercial water-cooled reactors where WABAs are Al_2O_3-B_4C clad in Zircaloy and BSGs are B_2O_3-SiO_2 clad in 304 stainless steel.

Table 2: Compositions of Westinghouse WABA and BSG.

Element/Isotope	WABA (Al_2O_3-B_4C) wt%	BSG (B_2O_3-SiO_2) wt%
^{10}B	1.968	0.699
^{11}B	8.992	3.207
Carbon	3.040	--
Oxygen	40.479	53.902
Aluminum	45.521	1.167
Silicon	--	37.586
Potassium	--	0.332
Sodium	--	2.837

Although lithium is not typically considered for use as a BA, it has been used as a BA to produce tritium for nuclear weapons via the $^6Li(n,\alpha)^3H$ reaction. The United States stopped producing tritium for nuclear weapons at its production facility in Savannah River in 1988. In the late 1990s, BAs were designed and implemented into commercial LWRs, as described in NUREG 1607, in the form of tritium-producing burnable absorber rods (TPBARs). The TPBAR design is similar to that of the WABA or BSG (see **Figure 5**). The BA within the TPBAR was composed of cylindrical lithium aluminate ($LiAlO_2$) pellets with enriched ^6Li content. The BA was surrounded by a zircaloy tritium getter to absorb free tritium gas. The getter was nickel plated to prevent oxidation, then clad in Type 316 stainless steel. Tritium decays into ^3He with a half-life of about 12.32 years. This isotope of helium has a thermal neutron absorption cross section of 5318 b.

Even though ^{3}He abundance in the TPBAR is small due to the slow decay of tritium, its impact on reactivity must also be considered throughout the BAs operational cycle due to its large thermal neutron absorption cross section.

3.3. Fabrication and Material Properties of Commercial Water-Cooled Reactor BAs

3.3.1. Gadolinia

UO_2-Gd_2O_3 fueled BAs are commercially produced by a variety of fuel vendors, including Westinghouse Electric Company, Framatome, and Siemens. They are used extensively in BWRs because of the lack of soluble boron options. The use of gadolinium oxide as a BA in commercial water-cooled reactors is particularly attractive because (a) several isotopes have large thermal neutron absorption cross sections and (b) the use of Gd_2O_3 within the solid fuel itself is permissible due to the absence of helium accumulation.

The Gd isotopes with large neutron absorption cross sections constitute about 30% of the natural abundance (see **Table 1**). An ideal BA not only is initially a strong enough absorber to compensate for the excess reactivity of fresh fuel, but also burns out at a desired rate, such that the BAs residual reactivity decrement is zero at the end of the fuel's operational cycle. One additional method of controlling these parameters is to control the isotopics of the BA, i.e., to enrich the Gd isotopes of odd mass number to a desired concentration. Theoretical evaluation of the fuel cycle extension potential via Gd enrichment has been demonstrated, though the ultimate economic benefits of this methodology depend ultimately on the additional cost of the processes used [42]. Laser enrichment of the odd Gd isotopes is possible because the total width of the isotope structure is substantially larger than the bandwidth of common pulsed dye lasers [43]. Even with broadband lasers (~3 GHz), enrichment of the neutron-absorbing isotopes ^{155}Gd and ^{157}Gd to greater than 50% has been demonstrated experimentally [43]. Although the needed quantity of enriched Gd is less than that of uranium, Gd laser enrichment processes are still costly [44, 45]. Gadolinium enrichment has been experimentally demonstrated using cation exchange chromatography, but this technology is very inefficient [45]. A collaboration between Exelon Corporation and Oak Ridge National Laboratory (ORNL) is in progress, funded through the Department of Energy (DOE) Gateway for Accelerated Innovation in Nuclear (GAIN) program, with the objective of commercializing the plasma enrichment of the odd Gd isotopes.

Gd_2O_3 can crystallize in five different phases: low-temperature cubic (C), monoclinic (B), hexagonal (A), hexagonal (H), and X-phase (X) [46]. The Gd_2O_3 cubic phase is stable until the monoclinic phase transition at 1200°C, followed by a hexagonal phase transition at 2100°C, which persists until melting at 2420°C. The ZrO_2-Gd_2O_3 system is relevant because ZrO_2 is often used a surrogate for UO_2. When considering the UO_2-Gd_2O_3 and ZrO_2-Gd_2O_3 systems, it is important to note that the acceptable Gd_2O_3 content is limited (typically up to about 10 wt% [47]) due to high residual reactivity resulting from high neutron-absorbing radioisotopes in its decay chain [48]. The UO_2-Gd_2O_3 system forms a stable solid solution with a fluorite structure until melting within this composition range [49, 50]. Therefore, a simple linear relationship between theoretical density and gadolinia content at room temperature exists as shown in **Equation 17** [51].

$$TD_{(U,Gd)O_2} = 10.962 - 0.031\eta \quad \textbf{(Eq. 17)}$$

where

TD = Theoretical maximum density of UO_2- ηGd_2O_3 ($g \cdot cm^{-3}$)
η = Gadolinia content (wt%)

UO_2-Gd_2O_3 composites can be fabricated as either a dispersion or a solid solution. If we only consider the low-temperature Gd_2O_3 cubic fluorite-type structure in which one-quarter of the O^{2-} ions are in the anion sublattice vacancy, one might assume that solid solutions of cubic fluorite-type (*Fm-3m*) structure would be stable in both the UO_2-Gd_2O_3 and ZrO_2-Gd_2O_3 systems [52]. For the surrogate binary system, however, Gd_2O_3 and ZrO_2 form eutectics with several phase transitions prior to melting, making thermophysical comparisons between the surrogate and the fuel composite difficult [46]. CeO_2 is also routinely used as a surrogate for UO_2 as well, and Gd_2O_3-doped ceria is an important oxygen-ion conductor in solid-oxide fuel cells [53]. CeO_2-Gd_2O_3 surrogates with gadolinia content below 20 wt% crystallize as a solid solution with fluorite structure at room temperature; however, a phase separation occurs between the range of 375°C (for 3 wt% gadolinia) to 725°C (for 10 wt% gadolinia), whereby the Gd_2O_3 forms C-type (*Ia-3*) nano- or micro-domains within the CeO_2 fluorite phase [53-55].

When incorporating pre-sintered Gd_2O_3 dispersoids into oxide fuel, the mismatch of densifications during sintering can produce excessive cracking between the BA and the fuel matrix. This can be ameliorated by controlling the initial density of the BA prior to sintering [47] or by doping the composite with a small amount (0.05 wt%) of TiO_2 [56]. A UO_2-Gd_2O_3 solid solution composite can be fabricated by co-precipitating the powders prior to pressing or sintering. The gadolinia can be distributed homogeneously throughout the UO_2 matrix by mixing uranium and gadolinium nitrates and adding a dilute ammonium hydroxide solution, then decomposing the mixture by heating in air and reduced in a hydrogen atmosphere [57, 58]. Co-precipitation [57, 59] and co-milling [52] methods result in greater final pellet densities than the commercially preferred conventional dry-blending method of the two oxide powders [60-63].

UO_2 nuclear fuel has been fabricated using the spark plasma sintering (SPS) method [64-66]. Recently, a UO_2-Gd_2O_3 composite was fabricated using the SPS method with varying gadolinia content, though microstructural, crystallographic, and thermal analyses of the resulting fuel were not conducted [67]. The addition of increasing gadolinia content resulted in decreasing compressive hardness, as well as increasing porosity [67]. Porosity should therefore be reduced with increasing SPS temperature by mitigating the Kirkendall effect [67-69].

Elastic property measurements of UO_2-ηGd_2O_3 are lacking in the peer-reviewed literature, particularly for dispersions of Gd_2O_3 in UO_2. The most recent elastic property measurements of solid solution UO_2-ηGd_2O_3, prepared using the coprecipitation technique, were taken in 1991 at room temperature using ultrasonic pulse-echo [70]. These measurements showed a linear

relationship between Young's modulus decrement and gadolinia content at room temperature, shown in **Equation 18** for 100% dense fuel, where $\eta < 20$ [70]. The Young's modulus of porous UO_2-Gd_2O_3 can be calculated via **Equation 19** and were determined at room temperature for porosity less than 10% [71]. It should be noted that this relationship is over half a century old, and the porosity correction in **Equation 19** is independent of composition (i.e., η value). This implies that the porosity correction should also apply to pure UO_2. Rather than 0.02277, the currently accepted porosity correction coefficient for pure UO_2 is 0.0262, which will be used in thermomechanical equations and calculations in forthcoming sections [72]. While the elastic properties of UO_2-ηGd_2O_3 as a function of gadolinia content, temperature, and porosity altogether have never been measured directly, models exist which attempt to predict the elastic properties as a function of all three parameters [73].

$$E_{(U,Gd)O_2} = E_{UO_2}\left(1-\eta\cdot 5.686\cdot 10^{-3}\right) \quad \textbf{(Eq. 18)}$$

Using a Young's modulus of 226 GPa for 100% dense pure UO_2 at 298 K [74] yields:

$$E_{(U,Gd)O_2}(\eta) = 226\left(1-\eta\cdot 5.686\cdot 10^{-3}\right)$$

where

η = Gadolinia content (wt%), $\eta \in (0,20)$

$E_{(U,Gd)O_2}(\eta)$ = Young's modulus (GPa) at 298 K, normalized to 100% theoretical density (TD)

$$E_{(U,Gd)O_2}(\eta,P) = 226\left(1-\eta\cdot 5.686\cdot 10^{-3}\right)\left(1-0.02277\cdot P\right)^{\text{a}} \quad \textbf{(Eq. 19)}$$

where

P = Porosity (%), $P \in (0,10)$

The thermal conductivity of nuclear fuel is an important parameter for reactor safety. Despite the relatively poor thermal conductivity of pure UO_2, the thermal conductivity of UO_2 at room temperature decreases further with increasing Gd_2O_3 content [75]. However, the decrement in thermal conductivity vs. BA content is less for Gd_2O_3 dispersions than Gd_2O_3 in solid solution with UO_2; this is attributed to less phonon-point defect scattering in the UO_2 matrix for the

[a] The porosity correction coefficient is independent of η, implying that it also applies to pure UO_2. The currently accepted porosity coefficient for pure UO_2 is 0.0262 (rather than 0.02277) and is recommended for use; however, the historical relationship using the 0.02277 coefficient is shown here.

dispersion fuel [76]. The thermal resistance at the boundary between the Gd_2O_3 dispersoids and the UO_2 also varies with temperature [76].

Historical data on the thermal conductivity of solid solution UO_2-ηGd_2O_3 vs. BA content exist from a variety of sources, including the Japan Atomic Energy Agency (formerly the Japan Atomic Energy Research Institute) [57], Framatome [77], Babcock and Wilcox [78], Exxon [79], and the Nippon Nuclear Fuel Development Company [75]. While all sources show the same general trend—that thermal conductivity decreases with increasing gadolinia content at room temperature—the data vary widely in magnitude below 2000 K depending on the source, and the difference in thermal conductivity from pure UO_2 is smaller above 2000 K [57, 75]. This relationship will be shown explicitly in a later section in comparison to other BAs.

3.3.2. Erbia

UO_2-ηEr_2O_3 BAs are commercially produced by Westinghouse Electric Company but are used less extensively than gadolinia or boron-based BAs due to fuel cycle cost considerations. Similar to gadolinium, the n,γ reaction for erbium BAs does not result in helium buildup, so the use of Er_2O_3 within the solid fuel itself is permissible. On a per-volume basis, however, the reactivity impact of Er_2O_3 is significantly less than that of Gd_2O_3 due to its smaller absorption cross section.

Erbia crystallizes in a C-type cubic structure at room temperature until the hexagonal phase transition at about 2320°C, just before melting at 2390°C [80, 81]. The crystallographic phase transitions of MO_2-Er_2O_3 surrogates are still largely unverified experimentally; however, recent studies suggest that their temperature-dependent properties and phase transitions are similar to that of Gd_2O_3 BA surrogates—i.e., fluorite solid solution at room temperature followed by high temperature C-type phase separations [82, 83].

Similar to gadolinia BAs, the general relationship describing change in surrogate lattice parameter vs. erbia content in single fluorite phase solid solution closely follows Vegard's law [84]. When the UO_2-Er_2O_3 composite is a single phase solid solution, a simple linear relationship exists between theoretical density and erbium content at room temperature, as shown in **Equation 20** [51]. However, recent evidence suggests that the UO_2-Er_2O_3 composite does not form a single phase solid solution [85]. Instead, X-ray diffraction (XRD) measurements reveal a second fluorite-type phase, the phase fraction of which increases and lattice parameter decreases with increasing erbia concentration [85].

$$TD_{(U,Er)O_2} = 10.962 - 0.0175\eta \qquad \textbf{(Eq. 20)}$$

where

TD = Theoretical maximum density of the UO_2-ηEr_2O_3 ($g \cdot cm^{-3}$)
η = Erbia content (wt%)

The simplest and most commercially favorable fabrication method of UO_2-ηEr_2O_3 is conventional dry mechanical blending, pressing, and sintering of composite powders. Assuming low erbia concentrations (<10 wt%), the composite forms a two-phase solid solution with a fluorite crystal structure when fabricated in the conventional manner if the sintering temperatures exceed 1500°C; however, the porosity of the final pellet can vary widely and is strongly dependent upon the quality of homogenization of the raw powders [85, 86]. While Er_2O_3 has been fabricated using SPS, UO_2-ηEr_2O_3 has not yet been fabricated using SPS at the time this paper was written.

The Young's modulus, lattice parameter, heat capacity, thermal conductivity, and thermal expansion coefficient of UO_2-Er_2O_3 as a function of temperature and BA concentration have been experimentally determined [74]. The thermomechanical relationships for UO_2-ηEr_2O_3 and UO_2-ηGd_2O_3 are similar when BA concentration is low. The UO_2-ηEr_2O_3 Young's modulus is linearly related to erbia content, as shown in **Equation 21**, for 100% dense fuel at room temperature where $\eta < 7$ [74]. The Young's modulus of porous UO_2-Er_2O_3 at room temperature can be calculated via **Equation 22** for porosity 10% or less [71]. The porosity correction coefficient 0.0262 should be used in **Equation 22** (rather than 0.02277) for the same reasoning as discussed in **Equation 19**.

$$E_{(U,Er)O_2}(\eta) = 226 - \frac{998.4\eta}{236.2+\eta} \qquad \textbf{(Eq. 21)}$$

where

η = Erbia content (wt%), $\eta \in (0,7)$

$E_{(U,Er)O_2}(\eta)$ = Young's modulus (GPa) at 298 K, normalized to 100% TD

$$E_{(U,Er)O_2}(\eta,P) = \left(226 - \frac{998.4\eta}{236.2+\eta}\right)(1-0.02277\cdot P)\ \text{[b]} \qquad \textbf{(Eq. 22)}$$

where

P = Porosity (%), $P \in (0,10)$

Similar to UO_2-ηGd_2O_3, the thermal conductivity of UO_2-ηEr_2O_3 decreases with increasing erbia content at room temperature, but this decrease is less noticeable above about 1500 K [74, 87]. This relationship will be shown explicitly in a later section in comparison to other BAs.

[b] The porosity coefficient of 0.0262 (rather than 0.02277) is recommended for use for the same reasoning as discussed in **Equation 19**.

3.3.3 Other Rare-Earth UO_2-M_2O_3 BAs

While other rare-earth BA oxides such as Dy_2O_3, Sm_2O_3, and Eu_2O_3 have been used historically as control rod materials, their commercial use as BAs is nearly nonexistent. All three oxide compounds form stable fluorite solid solutions or dispersions with UO_2 at room temperature, followed by a hexagonal phase transition near their melting points [88].

Experimental results from the 1960s indicate that UO_2-ηDy_2O_3, UO_2-ηSm_2O_3, and UO_2-ηEu_2O_3 can be fabricated in the conventional dry blending, pressing, and sintering of powders to form stable high-density dispersion fuels [89]. UO_2-ηEu_2O_3 was recently fabricated using SPS to form high density fluorite solid solution pellets, the properties and densification mechanisms of which were similar to those for UO_2-ηGd_2O_3 counterparts fabricated using SPS [67, 90].

3.3.4 ZrB_2

Zirconium borides were first experimentally considered for commercial LWR use in the Shippingport PWR in the late 1950s. In addition to the development of Zircaloy cladding, the experiments at Shippingport also attempted to demonstrate the use of zirconium-uranium-boron metallic fuel (which was rejected in favor of standard UO_2 fuel for commercial LWRs). In the Shippingport Core 1-Seed 2, BAs composed 90–96 wt% Zircaloy, 3.9–9.9 wt% uranium, and 0.03–0.11 wt% natural boron were fabricated and irradiated [91]. The metallic fuel BA consisted mostly of the α-zirconium and ε-zirconium-uranium hexagonal phases. However, because of its insolubility, the BA was distributed within the fuel matrix as a dispersion of ZrB_2, which also adopts a hexagonal crystalline structure. The BAs were fabricated by extrusion and hot or cold working of the alloys. The mechanical properties of the zirconium-uranium-boron alloys were found to be strongly affected by variations in both impurity content and fabrication parameters [91].

Zirconium diboride (ZrB_2) is an attractive BA material due to the low cost of boron, as well as the excellent thermophysical properties of ZrB_2. ZrB_2 has a melting point of about 3000°C. Its thermal conductivity is in the range of 70 – 100 $W \cdot m^{-1} \cdot K^{-1}$ below 2000°C [92, 93]. Recent studies have shown that while the lithium resulting from neutron absorption of ^{10}B remains retained within the ZrB_2 matrix, the helium released from the n,α reaction has a low diffusion activation energy; it therefore diffuses easily through the matrix, readily resulting in helium release [29]. The current commercial use of ZrB_2 is as a thin-film coating over pure UO_2 nuclear fuel (see **Figure 4**). The technology to coat UO_2 fuel with a thin film of ZrB_2 was developed by Westinghouse in the late 1980s; today the coating is deposited using physical vapor deposition from a ZrB_2 electrode [94].

3.3.5 Al_2O_3-B_4C Wet Annular Burnable Absorber

Another possible BA design, the WABA, offers a method of inserting initial negative reactivity to provide significant fresh fuel reactivity hold down without binding the BA onto or within the

fuel itself. Unlike control rods or boric acid in the coolant, WABAs are integral burnable absorbers because they are non-removable parts of the fuel assembly. A typical WABA, shown in **Figure 5**, is typically inserted into the top of fuel assembly guide thimble tubes. In current practice, Al_2O_3-B_4C WABAs are used in conjunction with IFBAs in order to more precisely optimize fresh fuel reactivity hold down while also controlling BA burnout and residual reactivity near the end of the fuel's operational cycle. The commercial design, such as the WABA produced by Westinghouse, comprises rods containing alumina pellets with boron carbide dispersoids, clad in Zircaloy, where the weight percent of B_4C and the number of WABAs per assembly are variable. The Al_2O_3-B_4C WABAs are fabricated via standard mixing, pressing, and sintering of powders [95].

Assuming the WABA maintains its structural integrity, post-irradiation examination (PIE) studies have shown the vast majority (>99%) of critical reaction productions, such as tritium, are retained and do not release into the plenum gas [96]. From a thermal safety perspective, there is no fuel in the WABA, so heat generation within this type of BA is less than in a fueled BA. As shown in **Figure 5**, however, water coolant flows around both the outside and inside surfaces of the WABA to remove heat released following the ^{10}B neutron absorption reaction. The diffusion of oxygen into the Zircaloy cladding occurs rapidly above 1500 °C [97]. The reaction products are partially liquid above this temperature, resulting in low temperature melt formation of the WABA/cladding system. This phenomenon may have contributed toward the severe damage in the upper end fittings of the burnable poison rod fuel assemblies during the Three Mile Island-2 accident [97].

3.4. Comparison of Thermomechanical Properties

3.4.1. Young's Modulus

Understanding BA thermomechanical properties as a function of temperature is important in order to predict fuel performance during normal and accident scenario conditions. Determining the temperature-dependent elastic properties of UO_2-ηM_2O_3 compounds is difficult due to a lack of high-temperature experimental data. It is also important to note that, ideally, the BA population should reach zero near EOC; this means that fueled BA thermophysical properties will change throughout the course of the fuel's operational cycle due to changes in composition. However, a methodology for predicting the temperature-dependent Young's modulus of UO_2-ηM_2O_3 compounds (E_{pellet}) can be realized as follows. If the elastic properties of the constituents of a composite material behave linearly with temperature (i.e., no phase changes, elastic coupling, etc.), as is the case for the UO_2 and M_2O_3 materials in the current discussion over a wide temperature range [98], and if the influence of porosity and temperature on the elastic properties of the solid are independent, then the Young's modulus of an isotropic composite solid can be approximated by the "rule of mixing"—i.e., the linear combination of the volume-weighted Young's moduli of its constituents, shown in **Equation 23** [99]. **Equation 23** assumes that the composite and its constituents are 100% TD. A porosity correction will be applied later. For this discussion, the composite constituents of interest are UO_2 and M_2O_3, where M is Gd, Er, or Sm.

$$E_{pellet,100} = E_{UO_2} V_{UO_2} + E_{M_2O_3} V_{M_2O_3} \quad \textbf{(Eq. 23)}$$

where

$E_{pellet,100}$ = temperature-dependent Young's modulus of the composite at 100% TD

E_{UO_2} = temperature-dependent Young's modulus of UO_2 at 100% TD

V_{UO_2} = volume fraction of UO_2 in the composite, assuming 100% TD

$E_{M_2O_3}$ = temperature-dependent Young's modulus of M_2O_3 at 100% TD

$V_{M_2O_3}$ = volume fraction of M_2O_3 in the composite, assuming 100% TD

The composition of materials is often expressed in terms of weight percent due to the ease of measuring the weights of the constituent raw powders during fabrication. The relationship in **Equation 23** can be expressed in terms of weight percent (for a composite solid at 100% TD) by using **Equation 24**.

$$E_{pellet,100} = E_{UO_2} \cdot \frac{\frac{WF_{UO_2}}{\rho_{UO_2}}}{\frac{WF_{UO_2}}{\rho_{UO_2}} + \frac{WF_{M_2O_3}}{\rho_{M_2O_3}}} + E_{M_2O_3} \cdot \frac{\frac{WF_{M_2O_3}}{\rho_{M_2O_3}}}{\frac{WF_{UO_2}}{\rho_{UO_2}} + \frac{WF_{M_2O_3}}{\rho_{M_2O_3}}} \quad \textbf{(Eq. 24)}$$

where,

$WF_{UO_2} = \frac{1-\eta}{100}$ = the weight fraction of UO_2 in the composite, assuming 100% TD

$\rho_{UO_2} = 10.962$ = the density of UO_2 at 100% TD [100]

$WF_{M_2O_3} = \frac{\eta}{100}$ = the weight fraction of M_2O_3 in the composite, assuming 100% TD

$\rho_{M_2O_3}$ = the density of M_2O_3 at 100% TD

M = the BA species (Gd, Er, or Sm)

Finally, a porosity correction can be included, as shown in **Equation 25**, which is valid when porosity is small (i.e., less than 10%) [72, 101]. In practice, the porosity correction varies depending on the material and composition (which also changes due to BA burnup). Note that the porosity correction coefficient of 0.0262 should be used in **Equation 25** for the same reasoning as discussed in **Equation 19** and **Equation 22**.

$$E_{pellet} = \left(E_{UO_2,100} \cdot \frac{\frac{WF_{UO_2}}{\rho_{UO_2}}}{\frac{WF_{UO_2}}{\rho_{UO_2}} + \frac{WF_{M_2O_3}}{\rho_{M_2O_3}}} + E_{M_2O_3,100} \cdot \frac{\frac{WF_{M_2O_3}}{\rho_{M_2O_3}}}{\frac{WF_{UO_2}}{\rho_{UO_2}} + \frac{WF_{M_2O_3}}{\rho_{M_2O_3}}} \right) (1 - 0.0262 \cdot P) \quad \textbf{(Eq. 25)}$$

where

E_{pellet} = the temperature-dependent porosity-dependent Young's modulus of the composite pellet
P = Porosity (%), $P < 10$

Obtaining the Young's modulus of a composite using **Equation 25** requires assembling the properties and relationships of its constituent components. The temperature-dependent Young's moduli of UO_2, Gd_2O_3, Er_2O_3, and Sm_2O_3 all follow the linear relationship shown in **Equation 26** between 298 and 1500 K where m and b are the coefficients provided in **Table 3** for each material at 100% theoretical density [72, 102-104].

$$E_n(T) = mT + b \quad \textbf{(Eq. 26)}$$

where

E_n = Young's modulus

m,b = material-specific coefficients (see **Table 3**)

T = Temperature

Table 3: Young's modulus vs. temperature coefficients in **Equation 26** for UO_2, Gd_2O_3, Er_2O_3, and Sm_2O_3 at 100% theoretical density.

Equation	Reference	Material	m (GPa·K^{-1})	b (GPa)
27	[72]	UO_2	-0.0256	233
28	[102]	Gd_2O_3	-0.0229	163
29	[103]	Er_2O_3	-0.0204	185
30	[104]	Sm_2O_3	-0.03	158

An example of fueled BA compositions and properties is given in **Table 4** where 10 wt% BA content has been assumed. By combining **Equations 25-30**, the Young's moduli for UO_2-ηGd_2O_3, UO_2-ηEr_2O_3, and UO_2-ηSm_2O_3 can be obtained over a wide range of temperatures, porosities, and

BA concentrations. These relationships are plotted in **Figure 6** for comparison, where η = 10 wt% and TD = 95% have been chosen. **Figure 7** shows the Young's modulus of UO_2-ηGd_2O_3 as a function of temperature to highlight the influence of BA additive content.

Table 4: Volume Fraction of UO_2-$10M_2O_3$ Constituents.

BA Additive	Wt %	ρ at 100% TD ($g \cdot cm^{-3}$)	BA Vol. Frac.	UO_2 Vol. Frac.
Gd_2O_3	10	8.348 [102]	0.127	0.873
Er_2O_3	10	8.651 [103]	0.123	0.877
Sm_2O_3	10	7.748 [104]	0.136	0.864

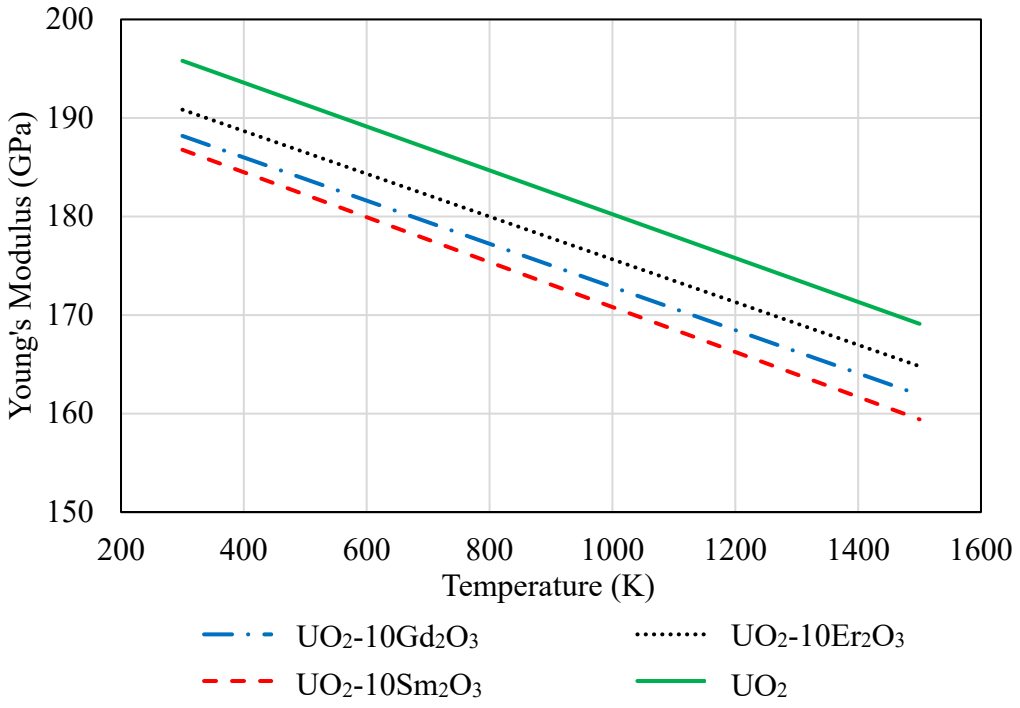

Fig. 6: The Young's moduli vs. temperature of unirradiated 95% TD UO_2 and 95% TD UO_2-$10M_2O_3$ as calculated using **Equations 25-30**.

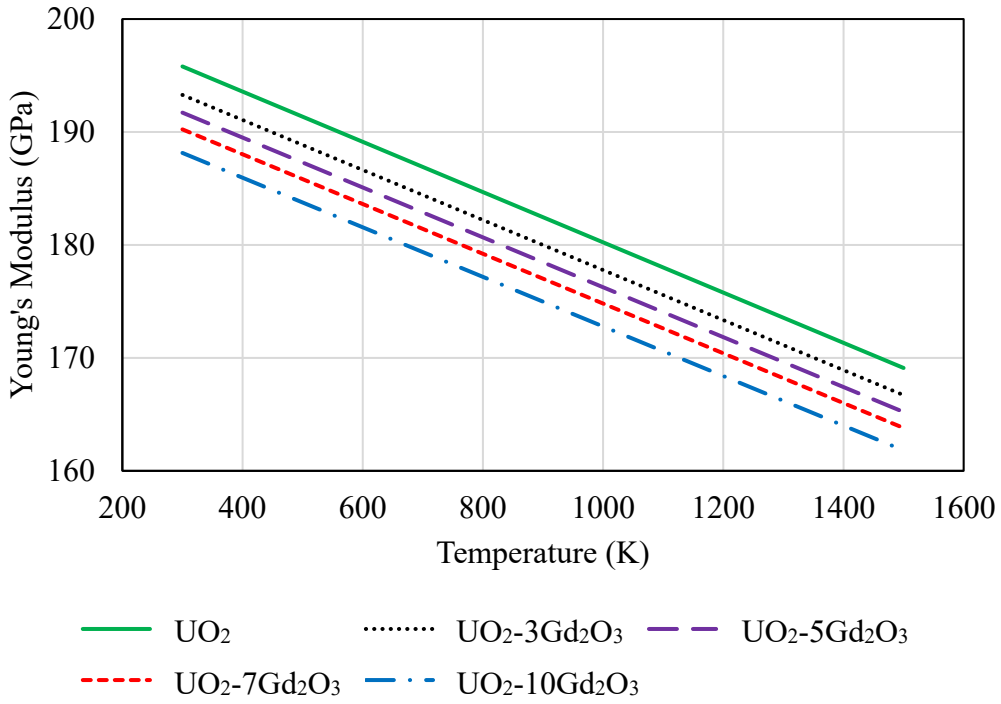

Fig. 7: The 95% TD UO_2-ηGd_2O_3 Young's moduli vs. temperature for varying BA contents as calculated using **Equations 25-28**, where η = 0, 3, 5, 7, and 10 wt%.

The Young's moduli vs. temperature illustrated in **Figure 6** and **Figure 7** show several important characteristics of the UO_2-M_2O_3 rare-earth BAs discussed in this section. From **Figure 6**, we see that the fuel stiffness is always reduced with increasing M_2O_3 BA content, regardless of which BA material is chosen. Second, **Figure 7** shows that increasing the BA content within the fuel further decreases the stiffness of the material. Finally, from both figures, increasing temperature always lowers the elastic stiffness of the materials regardless of composition.

Although UO_2 fuel coated with a ZrB_2 BA layer does constitute a fueled BA, it is assumed that the coating itself provides negligible benefit toward the mechanical integrity of the fuel due to the miniscule thickness of the layer in comparison to the size of commercial UO_2 fuel pellets. For this reason, the temperature-dependent Young's modulus of ZrB_2 is not included in **Figure 6**, but is provided independently in **Equation 31** and is valid from 273–2000 K [105]. **Equation 31** assumes a porosity of less than 5%.

$$E_{ZrB_2}(T) = 500 - 2.54Te^{-3273/T} + 1.9\left(T - 1188.1 + |T - 1188.1|\right)e^{-3273/T} \quad \textbf{(Eq. 31)}$$

where

T = Temperature (K)

3.4.2. Thermal Conductivity

Another important thermomechanical property for fueled BAs is thermal conductivity. In addition to UO_2-M_2O_3 and UB_2 (discussed in more detail in the next section) BAs, the thermal conductivity of ZrB_2 fuel coatings should also be considered because they are directly applied to the outer surface of the UO_2 fuel. As previously discussed, the addition of M_2O_3 BAs into UO_2 further decreases the fuel's thermal conductivity. Empirical relationships describing the thermal conductivity (κ) vs. temperature of pure UO_2 (95% TD) [106], UO_2-10Gd_2O_3 (95% TD) [75], UO_2-10Er_2O_3 (95% TD) [87], and ZrB_2 (100% TD) [92] in **Equation 32**, **Equation 33**, **Equation 34**, and **Equation 35**, respectively. The ZrB_2 thermal conductivity is reported here at 100% TD because the deposition techniques used to apply thin films can generally achieve >99% TD. The thermal conductivities of these materials are shown in **Figure 8**.

$$\kappa_{UO_2}\left(T\right)=\frac{100}{7.5408+17.692\cdot t_r+3.6142\cdot t_r^{\,2}}+\frac{6400}{t_r^{\,5/2}}\cdot e^{\frac{-16.35}{t_r}} \qquad \textbf{(Eq. 32)}$$

where

κ = thermal conductivity ($W\cdot m^{-1}\cdot K^{-1}$)

$t_r=\frac{T(K)}{1000}$ for temperatures between 273 and 2600 K.

$$\kappa_{UO_2-10Gd_2O_3}\left(T\right)=\frac{K_0}{x}\arctan\left(x\right)+3.57\cdot10^{-12}\cdot T^3 \qquad \textbf{(Eq. 33)}$$

where

$K_0=\left(2.35\cdot10^{-2}+2.55\cdot10^{-4}\cdot T\right)^{-1}$

$x=3.84\cdot\left(yK_0\right)^{1/2}\cdot e^{-9.65\cdot10^{-4}\cdot T}$

y = atomic fraction of Gd, valid from 0 to 0.142 (0 to 10 wt%)

$T\left(K\right)$ = for temperatures between 400 and 2023 K.

$$\kappa_{UO_2-10Er_2O_3}\left(T\right)=-7.954\cdot10^{-10}\cdot T^3+3.241\cdot10^{-6}\cdot T^2-5.731\cdot10^{-3}\cdot T+5.5 \qquad \textbf{(Eq. 34)}$$

where

$T\left(K\right)$ = for temperatures between 297 and 1700 K.

$$\kappa_{ZrB_2}(T) = 207.7 \cdot T^{-0.13372} \quad \textbf{(Eq. 35)}$$

where

$T(K)$ = for temperatures between 297 and 2300 K.

Figure 8 illustrates that UO_2 thermal conductivity is reduced with the incorporation of M_2O_3 BA material in the fuel, though this decrease is small for UO_2-$10Gd_2O_3$ at temperatures above 1500 K. ZrB_2 has significantly higher thermal conductivity than UO_2 or the UO_2-M_2O_3 composites.

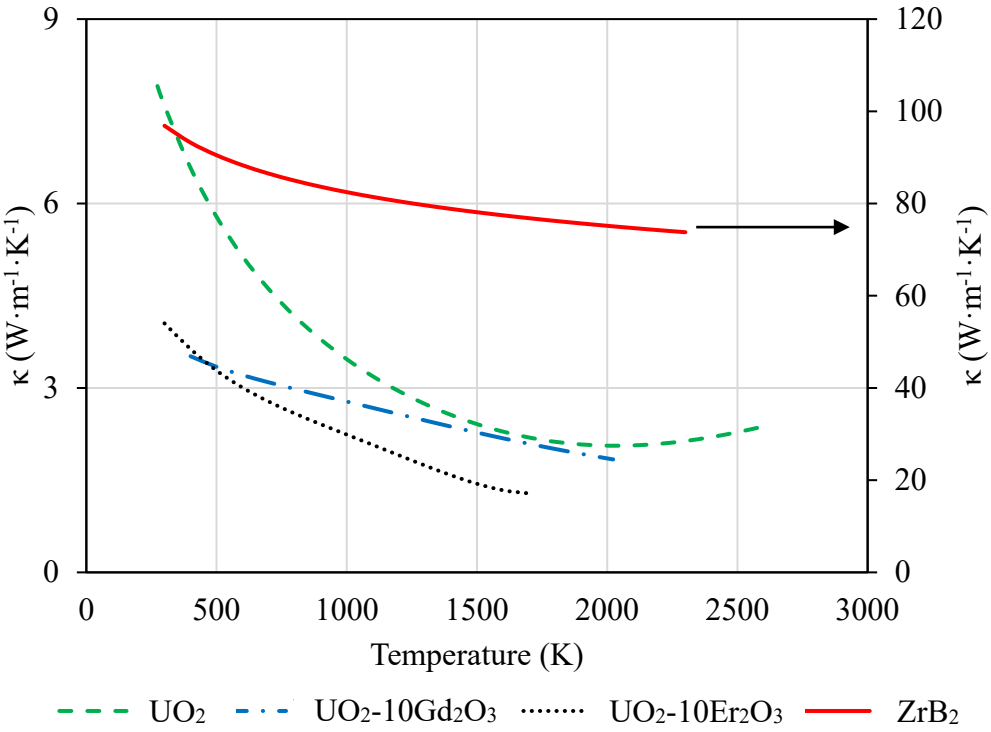

Fig. 8: Thermal conductivity vs. temperature of unirradiated UO_2 (95% TD), UO_2-$10Gd_2O_3$ (95% TD), UO_2-$10Er_2O_3$ (95% TD), and ZrB_2 (100% TD), from **Equations 32-35**.

4. Burnable Absorbers for Research and Test Reactors

Low power research reactors (e.g., AGN-201 [107], Argonaut [108]) rarely require burnable poisons as they are not designed for significant burnup and control rods provide sufficient reactivity control to offset reactivity change during operation. However, most higher power research and test rectors in the United States are intended to reach higher burnup and longer core

life, and they may have different neutron spectra than commercial water-cooled reactors. Research reactors are generally designed for producing neutrons for research applications but are often also used to produce special radioisotopes for medicine and industry, e.g., technetium-99m, cobalt-60, and americium-241. Most research reactors are also used for operational training. Test reactors, on the other hand, are generally used for materials testing and operate at higher flux levels, as well as production of radioisotopes. The US NRC classifies both as non-power reactors since they are not used for energy production. Such reactors contain varying fuel types (composition, shape, size, cladding) although all in the US are currently water cooled, but with different moderator and reflector materials. These features are varied according to the specific design application(s) of the reactor. Therefore, the nature of burnable poisons, when used, will vary by reactor type. Rather than attempt to describe each non-power reactor type and its use of burnable poisons, we will focus on some of the more common such designs and provide an overview of how BAs are deployed in those designs.

As of June 2021, the IAEA research reactor database [109] showed that there were 223 operational research and test reactors. 55 of these reactors are low power (less that 1 kW), primarily subcritical and critical assemblies but also including five AGN-201, eleven MNSR (Miniature Neutron Source Reactor), eight SLOWPOKE (Safe LOW-POwer Kritical Experiment)-type reactors (all located in Canada) and three Argonaut reactors; as noted earlier such systems do not typically use burnable absorbers. Of the remaining reactors, 38 are TRIGA (Training, Research, Isotopes, General Atomics)-type reactors. However, by far the most common reactor type, with various names and designers, are water-cooled plate-type reactors, most of which use Materials Test Reactor (MTR)-type fuel elements, manufactured worldwide (e.g., Argentina, Chile, Egypt, Germany, South Africa, the United Kingdom and the United States). All are believed to have been converted to LEU, but the fuel form varies by reactor, although most MTR-type fuels are based on uranium silicides. However, core configurations and BA usage varies widely depending on the purpose of the core. An in-depth survey of the various BA strategies for these reactors is beyond the scope of this paper; we will consider TRIGA and MTR-type designs, then conclude with a description of the Idaho National Laboratory's ATR and show how BA usage allows this reactor to operate in its designed high-flux regime.

4.1 TRIGA

The TRIGA class of reactors is the most widely used class of civilian research reactors in the United States and have been in use since the 1950s. Historically, there have been several different TRIGA reactor designs, such as the TRIGA Mark I, Mark II, Mark III, Mark F, etc. TRIGA reactors use uranium-zirconium hydride as fuel. The benefits of the $UZrH_x$ system (where x is the H:Zr ratio) include excellent chemical stability under the presence of hot water (making cladding failure accidents of no consequence), and high-temperature stability, particularly under large prompt-reactivity insertions. Early TRIGA designs originally used fuel with 8.5 to 12 wt% uranium content that was enriched to 20% ^{235}U. Directly above and below the $UZrH_x$ fuel meat, within the fuel rod, resided ~0.05 in. thick BA disks composed of Al_2O_3-Sm_2O_3. The samarium content of these disks varied up to about 1 wt%. While the BA disks did not improve the prompt

temperature coefficient, they did help compensate for reactivity changes during the fuel's operational cycle.

As higher TRIGA power levels and power densities became desirable, the uranium enrichment during the Fuel Life Improvement Program (FLIP) was increased to 70–93% while maintaining an 8.5–12 wt% uranium content. In order to offset the initial excess reactivity of the highly enriched uranium (HEU) FLIP fuel, 1–3 wt% erbium was incorporated into the $UZrH_{1.6}$ matrix, which acted as a BA. The erbium BA and its resonance peaks also contributed toward the prompt-negative temperature coefficient which changes very little due to burnup. The microstructure of TRIGA fuel, particularly after irradiation, is currently not well documented in the literature. Historically, the TRIGA fuel itself is fabricated by hydriding the U-Zr-Er solid solution alloy, during which the zirconium is preferentially hydride [110]. It is believed that the resulting microstructure takes the form of micro-scale dispersoids of uranium metal in the surrounding zirconium hydride matrix [111, 112]. In the 1970s, the FLIP fuel was replaced with its current 20% low-enriched uranium (LEU) fuel form at a much higher uranium content of 20–45 wt% and includes the erbium BA.

4.2 MTR-type Reactors

The original Materials Test Reactor used a highly-enriched uranium core made of metallic plate-type uranium-aluminum fuel clad in aluminum. Eighteen slightly curved rectangular plates of fuel were fitted into two aluminum side plates such that the assembled element had a rectangular cross section 8 cm × 7.6 cm. The side plates were 5 mm in thickness. Although the subsequent MTR-type reactors share the same basic fuel form factor, the reactor configurations and fuel meat/plate design vary by manufacturer, with fuel type determined largely by the manufacturer of the fuel.

The original Materials Test Reactor operated at what was then Argonne National Laboratory-West (present day Idaho National Laboratory) between 1952 and 1970. It was cooled and moderated by water and used a uranium-aluminum fuel clad in aluminum with highly enriched fuel. Although burnable absorbers were not initially employed, desire to operate longer cycles with higher power led to the addition of boron as a BA within the fuel meat. MTR was also used to test a number of different BA materials, including various boron compositions bonded with Zircaloy-2 [113] along with more esoteric BA materials such as Dy_2O_3 within the fuel matrix [114]. The Engineering Test Reactor (ETR), operated between 1957 through 1981, also used MTR-type plate fuel. In this core, the boron in the fuel meat was later moved to the aluminum side plates to flatten flux profiles in the core [114]. However, few of the remaining MTR-type cores need or utilize burnable absorbers at present. Among others, Japan's JRR-3M, Australia's OPAL and Argentina's RA10 research reactors use burnable absorbers in the form of thin cadmium wires placed in the sideplate of each fuel assembly [115-117]. Others use borated aluminium side plates like the original MTR, but most designs do not do not have the performance requriements that would make use of BAs desireable. For most research reactors, powers are sufficiently low that extension of fuel lifelime through burnable poisons was not a design requirement. However, there is ongoing work to assess the advantages and disadvantage of use of

BAs in MTR-type research reactors [118] and for the use of americium nuclides as a side plate loaded burnable poison in a MOX-loaded MTR-type 22 MW core [35].

4.3 Advanced Test Reactor

Like its predecessors (the MTR and the ETR), the ATR uses plate fuels to achieve the large power density needed for generating high fluxes for materials testing. While the MTR-type fuels used slightly curved plates in a rectangular fuel element, the ATR uses fuel plates swages into aluminum side plates and formed into wedge-shaped fuel elements with a 45° arc width, as illustrated in **Figure 9a**. In this element, fuel plates are numbered 1-19 beginning with the shortest plate (lower left in the figure) to the longest plate (top of the figure). The elements are arranged in the form of a four-lobed serpentine, as shown in **Figure 9b**. This configuration provides intense neutron fields within and between each of the four lobes, and in the center of the core, for a total of nine high-flux irradiation positions.

ATR uses aluminum-clad HEU fuel in the form of a uranium-aluminum mixture, as was used in its predecessors. Because innermost plates are shielded from thermal fluxes by the outermost plates, fission rates are highest in the outermost plates. To overcome this, in the current Mark 7 fuel assembly, plates 1-4 and 16-19 have BA added in the form of B_4C, combined with reduced inventories. Fuel/poison loadings are provided in **Table 5** [119]. This BA grading, combined with inverse fissile grading, serve to both flatten the fission profile across the element and to reduce the reactivity of the fresh fuel. After the first cycle (typically on the order of 60 days in ATR) the ^{10}B is essentially depleted; however, the reduced ^{235}U loading serves to maintain the flattened profile for subsequent cycles. Note that mass fractions are shown rather than actual mass, because the mass of each plate changes moving outward (from plate 1 to plate 19).

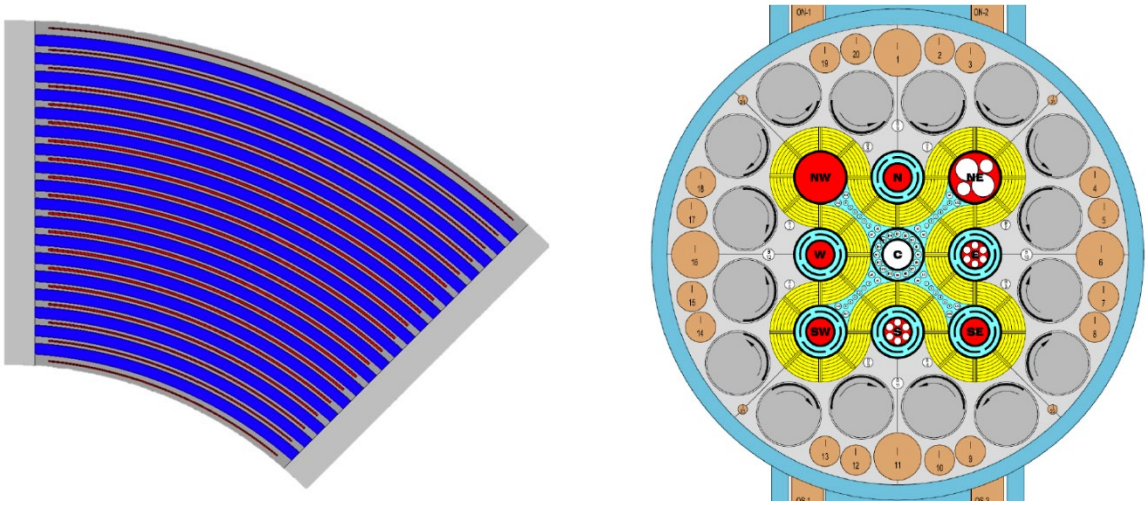

(a) (b)

Fig. 9: Illustrations of (a) an ATR fuel element design and (b) cross section of the ATR core. In 9a, the red regions represent fuel meat clad in aluminum (gray) and separated by water (blue). The fuel plates are swaged into the aluminum side plates (gray) to form the fuel element. In 9b,

40 fuel elements (shown in yellow) are arranged in a four-lobed serpentine pattern surrounded by rotating control drums (dark grey cylinders with arrows indicating rotation of hafnium poison, shown in black) and beryllium reflector (lighter grey). High-flux in-pile irradiation position are shown in red, safety rods in light blue, and outer experiment positions in orange.

Table 5: Isotopic mass fractions in ATR fresh fuel plates.

	Plate 1	Plate 2	Plate 3	Plate 4	Plates 5-15	Plate 16	Plate 17	Plate 18	Plate 19
^{10}B	0.07%	0.08%	0.04%	0.04%	0.00%	0.04%	0.04%	0.08%	0.08%
^{11}B	0.33%	0.34%	0.17%	0.17%	0.00%	0.17%	0.17%	0.34%	0.34%
^{12}C	0.11%	0.12%	0.06%	0.06%	0.00%	0.06%	0.06%	0.12%	0.12%
^{27}Al	68.45%	68.52%	63.26%	63.44%	58.23%	63.44%	63.47%	68.44%	68.67%
^{234}U	0.31%	0.31%	0.36%	0.36%	0.42%	0.36%	0.36%	0.31%	0.31%
^{235}U	28.86%	28.78%	33.92%	33.76%	38.85%	33.76%	33.74%	28.87%	28.64%
^{236}U	0.11%	0.11%	0.13%	0.13%	0.15%	0.13%	0.13%	0.11%	0.11%
^{238}U	1.75%	1.75%	2.06%	2.05%	2.36%	2.05%	2.05%	1.74%	1.74%

Figure 10 shows the radial fission density distribution, which is generally proportional to the power density. The hypothetical loading with neither BA nor graded fissile loading is shown in blue and illustrates significant peaking in outer plates caused by the self-shielding moving from the outer plates (e.g., 1, 2, 18, 19) to the inner plates (e.g., 9, 10, 11). However, the actual loading provided in **Table 5** for fresh fuel, plotted in orange in the figure, shows a much more flattened radial profile, with the power peak found in plate 15. This figure also shows the computed end of life power profile, in grey, where the eight initially borated plates are highly depleted and show a much lower fission density than the remainder of the element. For the boron-free element, the peak-to-average (P/A) fission density is 1.44; for the actual fuel with graded loadings, the P/A is 1.09 at beginning of life and 1.17 at end of life.

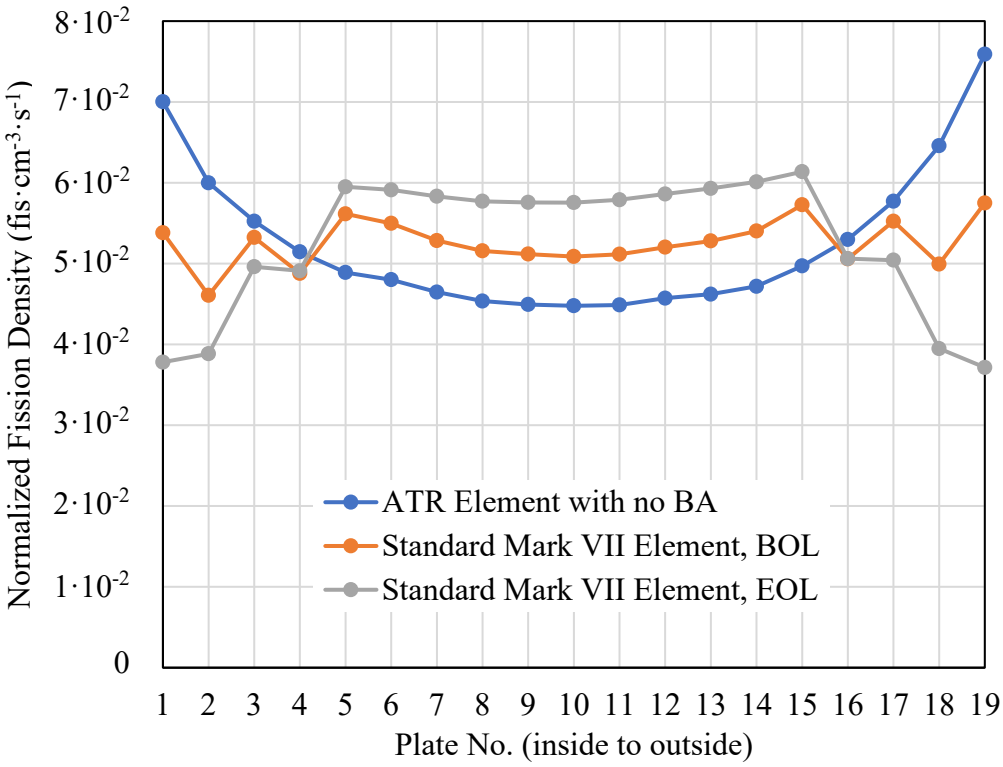

Fig. 10. Computed radial normalized fission density profiles with and without boron burnable absorber (error bars are on the order of the size of the symbols).

To highlight the behavior of borated fuel as a function of depletion, a model of the ATR loaded with all fresh fuel was simulated for a 180 day operational period (although, in practice, ATR is typically operated with a mix of fresh, once burned, and twice burned fuel, with a cycle length of 50-60 days). Control drums and shims used for core reactivity control [119] were not modified during the depletion simulation. From **Figure 11**, it is clear that, after the initial reactivity drop due to fission product poisoning (mostly xenon), the reactivity increase due to the depletion of ^{10}B is roughly equivalent to the negative reactivity due to fuel depletion for roughly 50 days. By this time, the ^{10}B content is approximately 30% of its initial density and no longer offsets the depletion of fissile material.

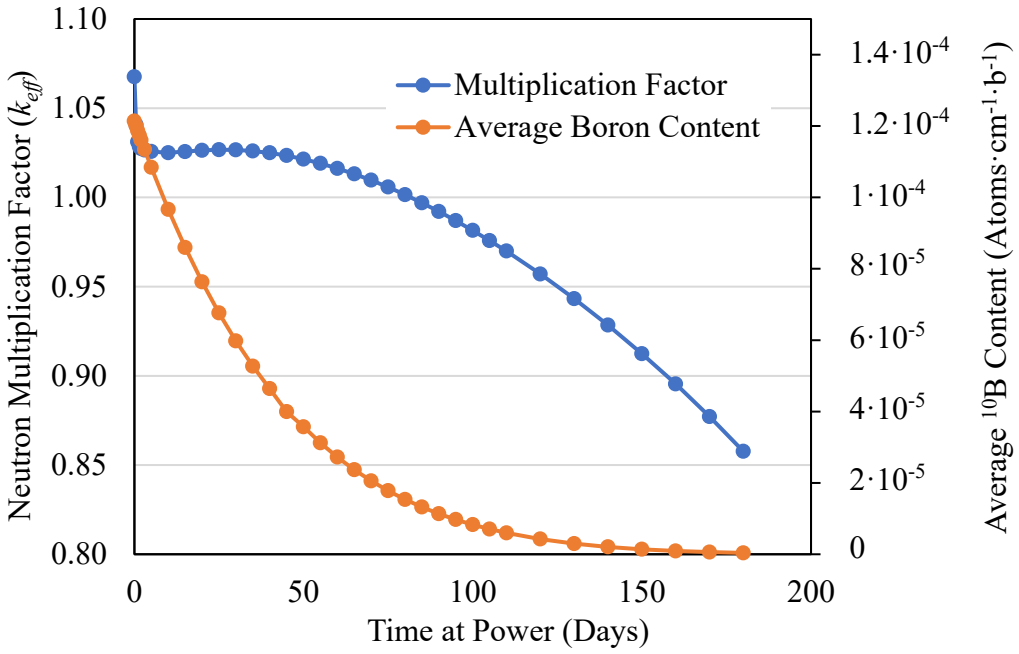

Fig. 11. Computed k_{eff} and average ^{10}B content for a core fully loaded with fresh fuel and depleted for 180 days (error bars are on the order of the size of the symbols).

Although the ATR is significantly different from other light water reactors, it provides an excellent demonstration of the use of BAs to offset fuel reactivity. For ATR fuel, a once-burned fuel assembly (50-60 days at power) loaded in the core will have almost the same reactivity as in its fresh state. However, with ^{10}B content reduced to less than 30% of its initial value, the reactivity of the fuel will decrease with burnup for its second and third cycles. Note that for a commercial reactor with less than 5 wt % enriched ^{235}U, production of fissile isotopes of plutonium helps to offset the loss of BA material with burnup.

5. Next-Generation Technologies

5.1. Thermal Spectrum Reactors

5.1.1 Uranium Diboride

The characterization and use of uranium diboride (UB_2) BAs was considered for nuclear reactors for over half a century [120, 121], though recently these studies have focused on computational efforts [122]. Uranium diboride has a hexagonal crystal structure (P6/mmm space group) and a melting point of about 2385°C [123]. Due to its higher density of 12.7 $g \cdot cm^{-3}$ in comparison to UO_2 (10.97 $g \cdot cm^{-3}$), UB_2 has a higher uranium density, which potentially allows for lower enrichment or longer fuel operational cycles from a criticality perspective.

Standard pressing and solid-state sintering of UB_2 powder typically does not yield high-density pellets. Hot pressing of powders has been attempted previously, but partial decomposition of UB_2 upon contact with graphite dies, as well as the formation of UB_4, UO_2, and UBC reaction byproducts have been observed [124]. UB_2 pellets were recently produced via arc melting and SPS to greater than 90% TD, but XRD of the resulting pellets suggest the presence of several impurity phases [123].

As previously mentioned, one unfavorable aspect associated with the use of UB_2 fuel is increased internal gas buildup resulting from the $^{10}B(n,\alpha)$ reaction. Due to the anisotropic nature of the hexagonal structure, swelling of UB_2 is also expected to occur anisotropically [125]. The anisotropic migration of defects is expected to reduce defect annihilation rates, meaning that the radiation tolerance of UB_2 is less than that of less anisotropic materials like UO_2 [125].

Temperature-dependent Young's modulus data for UB_2 are not well understood at high temperatures due to its affinity to oxidize in high temperature air, though UB_2 (95% TD) has been studied up to 673 K as shown in **Equation 36** [126]. An empirical relationship for the thermal conductivity of UB_2 (95% TD) is provided in **Equation 37** [123]. Note that the thermal conductivity of UB_2 (between 21 to 33 $W \cdot m^{-1} \cdot K^{-1}$ within the allowable temperature range) is much higher than the UO_2 and UO_2-M_2O_3 composites (see **Equations 32-35**).

$$E_{UB_2}(T) = -0.1019T + 339.98 \quad \textbf{(Eq. 36)}$$

where

$T(K)$ = temperatures between 297 and 673 K

$$\kappa_{UB_2}(T) = \frac{1}{A + BT} + \frac{T}{CT + D} + E \quad \textbf{(Eq. 37)}$$

where

$A = 9.586 \cdot 10^{-3}$

$B = 1.021 \cdot 10^{-4}$

$C = 153.4$

$D = -3.42 \cdot 10^{-2}$

$E = 5.958$

$T(K)$ = temperatures between 297 and 1773 K

5.1.2 Accident-Tolerant Fuel Candidates

A resurgence in the research and development of ATF candidates has occurred following the events of the Fukushima Daiichi disaster in 2011. An ideal ATF has higher thermal conductivity in comparison to standard UO_2 in order to improve safety during loss of coolant or loss of flow accidents while also having higher uranium density [100, 127]. Even though common ATF candidates like UN, U_3Si_2, and composites thereof suffer from catastrophic hydrolysis when in contact with high-temperature water consistent with commercial LWR design basis accidents [128-130], some of these fuels are still under consideration as dispersions or in other reactor types (gas-cooled reactors, lower temperature research reactors, etc.).

One such ATF-BA candidate is U_3Si_2-UB_2. Attempts to fabricate this composite using standard mixing, pressing, and sintering of powders have been unsuccessful, resulting in pellet densities of only 70–80% TD [131]. This could be due to the dissimilarity in bonding between the ionic-dominant UB_2 [132] and covalent-dominant U_3Si_2 [133], as has been observed (and resolved via other densification techniques) in other U_3Si_2 composites [100, 134, 135]. Within the low-density pellets, the U_3Si_2 and UB_2 phases appear to be stable in contact with each other up to 1500°C [131]. The relationship between UB_2 content within the U_3Si_2 and thermal conductivity, swelling, and fission gas release are still experimentally undetermined.

Another ATF-BA candidate is U_3Si_2 with gadolinium or gadolinia solid solutions or dispersoids. Implementing Gd into ATF candidates for use in thermal spectrum reactors might be highly desirable due to the historical success of UO_2-ηGd_2O_3 compounds. However, a variety of methods used to produce gadolinium doped U_3Si_2, including arc melting methods and powder blending, have thus far failed to produce structurally robust ATF-BAs [136].

The thermophysical properties of these ATF-BA composites have never been experimentally determined. The elastic properties of UN [137] or U_3Si_2 [126] ATF-BA composites can be calculated using **Equation 25** (note that the porosity correction factor of the ATF-BA will be different than that of UO_2's). The thermal conductivities of ATF-BA composites are generally more difficult since they are path-dependent rather than mass/volume-dependent, i.e., the simple rule of mixing is generally a poor approximation of a composite's thermal conductivity behavior. Instead, with the known thermal conductivities of the constituent materials, one may use the Maxwell approach to predict the thermal conductivity of the composite as described here [127].

5.1.3 Tristructural Isotropic Fuel

Tristructural isotropic (TRISO) fuel was originally conceived and designed to be a robust fuel for use in high-temperature gas-cooled reactors (HTGRs). As such, most studies have focused on HTGR applications of TRISO fuel. We note, however, that TRISO fuel boasts safety and performance characteristics that may benefit a variety of advanced reactor designs. The general design of TRISO fuel—as investigated under the U.S. DOE Advanced Gas Reactor (AGR) Fuel Development and Qualification Program—is illustrated below in **Figure 12** [138]. Multiple studies have demonstrated the benefits of implementing BAs in HTGRs in order to control the high excess reactivity associated with the fresh fuel configuration [139-142]. The use of BAs in HTGRs is also

important for thorium-fueled systems because they can dramatically reduce reactivity and flatten the reactivity swing to decrease the burden on the control rod mechanism, as well as reduce the positive temperature coefficient or even make it negative [143]. With the continued success of TRISO fuel, one may naturally consider the possibility of adding a fourth layer with BA material onto the fuel particle. While there is no evidence in the peer reviewed literature that this "quadruple isotropic" (QUADRISO) fuel concept has ever been experimentally attempted, neutronic studies suggest that the greatest operational lifetime for the same initial excess reactivity is achieved by using gadolinia-doped fuel in PWRs [144] while a combination of B_4C, CdO, and Gd_2O_3 could achieve similar results in HTGRs [145].

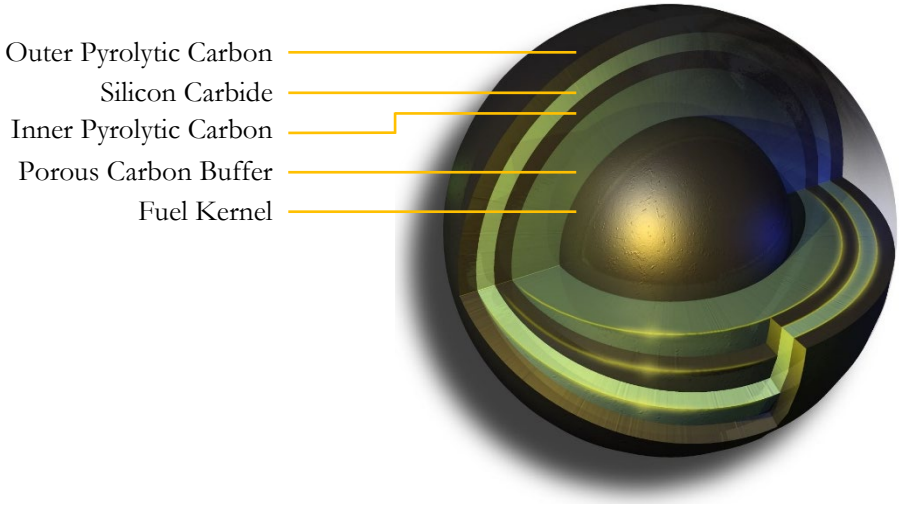

Fig. 12: Illustration of a TRISO fuel particle composed of a UCO fuel kernel surrounded by a porous graphite buffer layer, an inner pyrolytic carbon (IPyC) layer, a silicon carbide layer which acts as the primary pressure vessel, and a dense outer pyrolytic carbon (OPyC) layer. The QUADRISO fuel concept has been proposed which includes a fourth layer containing BA material.

5.2 Fast Spectrum Reactors

The benefits and uses of BAs for fast spectrum reactors are quite different than for thermal spectrum nuclear reactors. One distinct difference between fast vs. thermal spectrum reactors is the possibility for fast reactors to convert ^{238}U into fissile ^{239}Pu faster than the fuel is consumed—to have a breeding ratio (BR) greater than unity. For example, the BR for the Phénix sodium-cooled fast reactor (SFR) was measured as 1.16 [146]. This means that the fissile inventory in the reactor core increases with time. While thermal spectrum reactors can have a BR greater than unity (e.g., when using the thorium conversion cycle), strong neutron poison fission products are unavoidable for thermal spectrum reactors. The neutron-poisoning effect from fission products is

much smaller in fast spectrum reactors due to low neutron-absorption cross sections in the fast spectrum, where the important metric is the fission-to-capture ratio which is much larger in a fast spectrum reactor than in a thermal spectrum reactor.

Fast reactors can exhibit high burnup reactivity loss that leads to high excess reactivity and potential fuel melting in control rod withdrawal (CRW) accidents, which becomes an important constraint on the system's safety and efficiency [147]. By implementing, for example, Gd_2O_3-based BAs, fast reactor core inherent safety is improved by producing a larger margin to fuel melting in unprotected CRW accidents [147]. Low-enriched boron-based BA's are the most promising candidates for use in SFRs due to their impact on reactivity feedback coefficients from the low-Z materials, which more effectively slow down neutrons due to scattering [148]. Further, the $^{10}B(n,2\alpha)^3H$ cross section is substantially larger for fast neutrons, exceeding that of the $^{10}B(n,\alpha)$ cross section in the MeV range. However, there are proposed fast reactor designs that actually show an increase in reactivity from BOC to EOC [149-151]. This is also true of reactors that are typically designed for the express purpose of breeding, but the increase in excess reactivity is usually tempered by short cycles and extraction of the breeding blanket for processing. Some special purpose fast reactors, e.g., "burner" reactors [152, 153], by definition have a fairly large reactivity loss from cycle to cycle and, consequently, would benefit from the use of BAs.

6. Summary

This manuscript describes the potential benefits, challenges, and developmental efforts associated with burnable absorbers from a historical perspective, in current practice, and future potential. Several BAs are compared on the basis of their nuclear properties, fabrication methods, thermomechanical properties, and designs. BAs have many potential uses, such as the extension of the nuclear fuel's operational lifetime, safety and criticality control, the production of tritium for nuclear weapons, and the burning of long-lived radionuclides. Regardless of the intended purpose of the BA, its impact on reactivity must be considered. In thermal spectrum reactors, the BAs impact on reactivity can vary strongly based on its physical geometry and dimensions due to self-shielding effects.

Improvements in gadolinium- and boron-based BAs for use in the current reactor fleet will likely continue incrementally due to their historically extensive use in commercial LWRs. Improvements may include an ability to more accurately optimize the BA's burnout rate and impact on reactivity to further extend the fuel cycle. The combined use of boron and gadolinium appears attractive for development because of their contrasting burn rates. Current commercial LWR BA research efforts include the development of more efficient and affordable enrichment methodologies of highly neutron-absorbing isotopes for BAs, such as the gadolinium isotopes with odd atomic numbers.

Research reactors typically operate at much lower temperatures and power densities than commercial reactors. Research reactors also use different fuel (U-10Zr, U-10Mo, etc.) than commercial LWRs, such that their BAs have a different set of neutronic and thermophysical property requirements. Recent studies for the implementation of BAs in research reactors are

ongoing as part of the Reduced Enrichment for Research and Test Reactors (RERTR) and High Performance Research Reactor (HPRR) Programs under the DOE Office of Material Management and Minimization within the National Nuclear Security Administration (NNSA).

There are several opportunities for the R&D of BAs for use in advanced reactor systems. For example, QUADRISO fuel has been proposed, which adds an additional BA layer to the standard TRISO fuel design. Alternatively, it may be more straightforward to include a dispersion of burnable absorbers into the carbon matrix compact or the fuel kernel without the need to alter the TRISO layers. In this case, however, care must be taken to ensure that the gaseous products of the BA do not accumulate to compromise the structural integrity of the compact. In addition to helium accumulation from boron-based BAs, rare-earth oxide BAs, such as Gd_2O_3, might also contribute to the internal pressure of the compact due to oxygen interactions with the carbon matrix, resulting in carbon monoxide accumulation. Rare-earth carbide burnable absorbers may resolve this issue, though there is no evidence of experimental characterization of these materials at the time this manuscript was written. Several U_3Si_2-based BAs have also been proposed, but have yet to achieve a structurally robust, >95% dense ATF-BA. BAs can be beneficial in fast spectrum reactors as well, particularly for “burner” reactor designs, but their experimental demonstration in the peer-reviewed literature is extremely limited.

Acknowledgements

This manuscript has been authored by Battelle Energy Alliance, LLC, under Contract No. DE-AC07-05ID14517 with the U.S. Department of Energy. The United States Government retains and the publisher, by accepting the article for publication, acknowledges that the United States Government retains a nonexclusive, royalty-free, paid-up, irrevocable, world-wide license to publish or reproduce the published form of this manuscript, or allow others to do so, for United States Government purposes.

References

[1] V.I. Pavlov, V.D. Sidorenko, N.E. Pozdnyakov, Effectiveness of Using Burnable Absorbers in a Vver-1000, Atom Energy+ 73(6) (1992) 977-980.
[2] W.H. Bachman, R.P. Harris, R.A. Matzie, Fuel-Cycle Optimization with Integral Burnable Absorbers, T Am Nucl Soc 47 (1984) 68-70.
[3] F.J. Frank, L.R. Scherpereel, Incentives for Improved Burnable Absorber Designs, T Am Nucl Soc 40 (1982) 191-194.
[4] P.K. Doshi, W.L. Orr, D. Rombouts, Improved Fuel Utilization through Advanced Burnable Absorbers, T Am Nucl Soc 40 (1982) 188-191.
[5] G.A. Sofer, Technology of Burnable Absorber Reactivity Control and Other Techniques to Increase Fuel Burnup in Lwr Fuel-Cycles, T Am Nucl Soc 40 (1982) 183-184.
[6] F.B. Skogen, R.B. Stout, G.A. Sofer, Experience with Gadolinia Burnable Absorbers in Light Water-Reactors, T Am Nucl Soc 39 (1981) 401-402.

[7] D. Lanning, D. Baldwin, M. Cunningham, S. Marschman, Postirradiation Examination Report for the Tritium-Producing Burnable Absorber Rods Irradiated in the Watts Bar Nuclear Plant, in: U.S. Nrc (Ed.) Pacific Northwest National Laboratory, 2002, p. 72.
[8] E.P. Naessens, K.S. Allen, B.E. Moretti, Use of Pu-240 Waste as a Burnable Absorber in Light Water Reactors, Nucl Sci Eng 152(3) (2006) 306-313.
[9] I. Shaaban, M. Albarhoum, The Use of Mox Caramel Fuel Mixed with Am-241, Am-242m and Am-243 as Burnable Absorber Actinides for the Mtr Research Reactors, Appl Radiat Isotopes 125 (2017) 188-195.
[10] W. Häfele, D. Faude, A. E a Fischer, H.J. Laue, Fast Breeder Reactors, Annual Review of Nuclear Science 20(1) (1970) 393-434.
[11] R. Burn, Introduction to Nuclear Reactor Operations, Detroit Edison Company, Detroit, Michigan, 1982.
[12] The Shippingport Pressurized Water Reactor, U.S. Atomic Energy Commission, Addison-Wesley Publishing Company1958.
[13] Iaea-Tecdoc-1132, Control Assembly Materials for Water Reactors: Experience,

Performance and Perspectives, IAEA, 1998.
[14] K. Yuan, R.C. Ewing, U. Becker, Thermodynamic Mixing Properties of the Uo2-Hfo2 Solid Solution: Density Functional Theory and Monte Carlo Simulations, J Nucl Mater 458 (2015) 296-303.
[15] A.B. Mukhopadhyay, J.F. Sanz, C.B. Musgrave, First-Principles Investigation of Hydroxylated Monoclinic Hfo2 Surfaces, Chem Mater 18(15) (2006) 3397-3403.
[16] N.W. Pi, M.H. Zhang, J.C. Jiang, A. Belosludtsev, J. Vlcek, J. Houska, E.I. Meletis, Microstructure of Hard and Optically Transparent Hfo2 Films Prepared by High-Power Impulse Magnetron Sputtering with a Pulsed Oxygen Flow Control, Thin Solid Films 619 (2016) 239-249.
[17] Y. Aoki, T. Kunitake, A. Nakao, Sol-Gel Fabrication of Dielectric Hfo2 Nano-Films; Formation of Uniform, Void-Free Layers and Their Superior Electrical Properties, Chem Mater 17(2) (2005) 450-458.
[18] S. Tongpeng, K. Makbun, P. Peanporm, R. Sangkorn, O. Namsar, P. Janphuang, S. Pojprapai, S. Jainsirisomboon, Fabrication and Characterization of Hafnium Oxide Thin Films, Mater Today-Proc 17 (2019) 1555-1560.
[19] J.R. Deen, J.L. Snelgrove, Advantages of Cadmium Burnable Absorbers in Research and Test Reactors, T Am Nucl Soc 38(Jun) (1981) 287-288.
[20] N. Ghazi, H.H. Hassan, A. Hainoun, Core Conversion Analyses of the Syrian Mnsr Reactor from Heu to Leu and Meu Fuel with Homogeneously Mixed Burnable Poisons, Appl Radiat Isotopes 67(10) (2009) 1919-1924.
[21] S. Kalcheva, G.V.D. Branden, Preparatory Studies for Qualification of Lead Test Assemblies with Gadolinium as Burnable Absorber in the Br2 Reactor, International Conference on Mathematics & Computational Methods Applied to Nuclear Science & Engineering, Korean Nuclear Society, Jeju, Korea, 2017.
[22] N. Franck, S. Kalcheva, E. Koonen, Cd Wires as Burnable Poison for the Br2 Fuel Element, Proceedings of the 13th International Topical Meeting on Research Reactor Fuel Management, Vienna, Austria, 2009.
[23] S. Kalcheva, G.V.D. Branden, E. Koonen, Reactivity Performance of Two Prototypes Heu Fuel Elements with Cadmium Wires Irradiated in the Br2 Reactor, Proceedings of the 16th

International Topical Meeting on Research Reactor Fuel Management, Prague, Czech Republic, 2012.
[24] W. Chubb, Cadmium Oxide Glazed Nuclear Fuel Pellet and Glazing Composition, in: U. States (Ed.) CBS Corp, United States, 1986.
[25] I. Glagolenko, D. Wachs, N. Woolstenhulme, G. Chang, B. Rabin, C. Clark, Irradiation Testing of the Rertr Fuel Miniplates with Burnable Absorbers in the Advanced Test Reactor, RERTR 2010 — 32nd Internation Meeting On Reduced Enrichment For Research And Test Reactors, Argonne National Laboratory, Lisbon, Portugal, 2010.
[26] J. Cetnar, General Solution of Bateman Equations for Nuclear Transmutations, Ann Nucl Energy 33(7) (2006) 640-645.
[27] A. Radkowsky, Theory and Application of Burnable Poisons, Proceedings of the Second United Nations International Conference on the Peaceful Uses of Atomic Energy, Vol. 13 - Reactor Physics and Economics, United Nations, Geneva, 1958, pp. 426-445.
[28] F. Franceschini, B. Petrovic, Fuel with Advanced Burnable Absorbers Design for the Iris Reactor Core: Combined Erbia and Ifba, Ann Nucl Energy 36(8) (2009) 1201-1207.
[29] S.C. Middleburgh, D.C. Parfitt, P.R. Blair, R.W. Grimes, Atomic Scale Modeling of Point Defects in Zirconium Diboride, J Am Ceram Soc 94(7) (2011) 2225-2229.
[30] V.S. Volkov, A.S. Luk'yanov, V.V. Chapkunov, V.P. Shevyakov, V.S. Yamnikov, Use of Burnable Poisons in Nuclear Reactors, Soviet J. Atomic Energy 11(2) (1962) 109-125.
[31] M.B. Chadwick, M. Herman, P. Oblozinsky, M.E. Dunn, Y. Danon, A.C. Kahler, D.L. Smith, B. Pritychenko, G. Arbanas, R. Arcilla, R. Brewer, D.A. Brown, R. Capote, A.D. Carlson, Y.S. Cho, H. Derrien, K. Guber, G.M. Hale, S. Hoblit, S. Holloway, T.D. Johnson, T. Kawano, B.C. Kiedrowski, H. Kim, S. Kunieda, N.M. Larson, L. Leal, J.P. Lestone, R.C. Little, E.A. Mccutchan, R.E. Macfarlane, M. Macinnes, C.M. Mattoon, R.D. Mcknight, S.F. Mughabghab, G.P.A. Nobre, G. Palmiotti, A. Palumbo, M.T. Pigni, V.G. Pronyaev, R.O. Sayer, A.A. Sonzogni, N.C. Summers, P. Talou, I.J. Thompson, A. Trkov, R.L. Vogt, S.C. Van Der Marck, A. Wallner, M.C. White, D. Wiarda, P.C. Young, Endf/B-Vii.1 Nuclear Data for Science and Technology: Cross Sections, Covariances, Fission Product Yields and Decay Data, Nucl Data Sheets 112(12) (2011) 2887-2996.
[32] M. Zeman, R. Skoda, J. Zavorka, Epr: Burnable Absorber Optimization, Proceedings of the 26th International Conference on Nuclear Engineering, 2018, Vol 9 (2018).
[33] A. Dandi, M. Lee, M.H. Kim, Feasibility of Combinational Burnable Poison Pins for 24-Month Cycle Pwr Reload Core, Nucl Eng Technol 52(2) (2020) 238-247.
[34] C. Vandenberg, H. Bonet, A. Charlier, F. Motte, Safety Aspects of Using Gadolinium as Burnable Poison in Pressurized Water-Reactors, Nucl Technol 46(3) (1979) 500-506.
[35] I. Shaaban, M. Albarhoum, A Computational Study of Re-Cycling the Mtr Research Reactors with Mox Fuel Mixed with Am-241, Am-242 and Am-243 as Burnable Absorbers Actinides Using the Mcnp4c Code, Ann Nucl Energy 109 (2017) 626-634.
[36] H. Guo, T. Kooyman, P. Sciora, L. Buiron, Application of Minor Actinides as Burnable Poisons in Sodium Fast Reactors, Nucl Technol 205(11) (2019) 1447-1459.
[37] M. Tonks, D. Andersson, R. Devanathan, R. Dubourg, A. El-Azab, M. Freyss, F. Iglesias, K. Kulacsy, G. Pastore, S.R. Phillpot, M. Welland, Unit Mechanisms of Fission Gas Release: Current Understanding and Future Needs, J Nucl Mater 504 (2018) 300-317.
[38] B.V. Haibach, M.A. Feltus, A Study on the Optimization of Integral Fuel Burnable Absorbers Using Deterministic Methods, Ann Nucl Energy 24(11) (1997) 835-846.

[39] M.S. Yahya, Y. Kim, Burnable Absorber-Integrated Guide Thimble (Bigt) - Ii: Application to 3d Pwr Core Design, J Nucl Sci Technol 53(10) (2016) 1521-1527.
[40] M.S. Yahya, H. Yu, Y. Kim, Burnable Absorber-Integrated Guide Thimble (Bigt) - I: Design Concepts and Neutronic Characterization on the Fuel Assembly Benchmarks, J Nucl Sci Technol 53(7) (2016) 1048-1060.
[41] C.V. Parks, J.C. Wagner, Parametric Study of the Effect of Burnable Poison Rods for Pwr Burnup Credit, Nureg/Cr-6761, Ornl/Tm-2000/373, in: O.O.N.R.R. U.S. Nuclear Regulatory Commission (Ed.) U.S. Nuclear Regulatory Commission, Washington, DC, 2002.
[42] D. Campolina, E.F. Faria, A.a.C. Santos, V. Vasconcelos, M.P.V. Franco, M.S. Dias, J.R.L. Mattos, Parametric Study of Enriched Gadolinium in Burnable Neutron Poison Fuel Rods for Angra-2, Ann Nucl Energy 118 (2018) 375-380.
[43] M.I.K. Santala, H.M. Lauranto, T.T. Kajava, R.R.E. Salomaa, Laser-Enrichment of the Odd Isotopes of Gadolinium for Use as Burnable Poison in Nuclear Reactors, Aip Conf Proc (329) (1995) 237-240.
[44] K. Ogura, T. Arisawa, T. Shibata, Ion Collection from Laser-Induced Plasma Using Positively Biased Wire Electrode, Jpn J Appl Phys 1 31(5a) (1992) 1485-1490.
[45] J.R. Chen, M. Nomura, Y. Fujii, F. Kawakami, M. Okamoto, Gadolinium Isotope-Separation by Cation-Exchange Chromatography, J Nucl Sci Technol 29(11) (1992) 1086-1092.
[46] S. Lakiza, O. Fabrichnaya, C. Wang, M. Zinkevich, F. Aldinger, Phase Diagram of the Zro2-Gd2o3-Al2o3 System, J Eur Ceram Soc 26(3) (2006) 233-246.
[47] Q.M. Mistarihi, W. Park, K. Nam, M.S. Yahya, Y. Kim, H.J. Ryu, Fabrication of Oxide Pellets Containing Lumped Gd2o3 Using Y2o3-Stabilized Zro2 for Burnable Absorber Fuel Applications, Int J Energ Res 42(6) (2018) 2141-2151.
[48] J. Choe, H.C. Shin, D. Lee, New Burnable Absorber for Long-Cycle Low Boron Operation of Pwrs, Ann Nucl Energy 88 (2016) 272-279.
[49] R.J. Beals, J.H. Handwerk, B.J. Wrona, Behavior of Urania-Rare-Earth Oxides at High Temperatures, J Am Ceram Soc 52(11) (1969) 578-&.
[50] R.J. Beals, J.H. Handwerk, Solid Solutions in System Urania-Rare-Earth Oxides - I Uo2-Gdo1.5, J Am Ceram Soc 48(5) (1965) 271-&.
[51] A.V. Fedotov, E.N. Mikheev, A.V. Lysikov, V.V. Novikov, Theoretical and Experimental Density of (U, Gd)O-2 and (U, Er)O-2, Atom Energy+ 113(6) (2013) 429-434.
[52] S.M. Ho, K.C. Radford, Structural Chemistry of Solid-Solutions in the Uo2-Gd2o3 System, Nucl Technol 73(3) (1986) 350-360.
[53] A. Kossoy, Q. Wang, R. Korobko, V. Grover, Y. Feldman, E. Wachtel, A.K. Tyagi, A.I. Frenkel, I. Lubomirsky, Evolution of the Local Structure at the Phase Transition in Ceo2-Gd2o3 Solid Solutions, Phys Rev B 87(5) (2013).
[54] C. Artini, G.A. Costa, M. Pani, A. Lausi, J. Plaisier, Structural Characterization of the Ceo2/Gd2o3 Mixed System by Synchrotron X-Ray Diffraction, J Solid State Chem 190 (2012) 24-28.
[55] P.A. Zguns, A.V. Ruban, N.V. Skorodumova, Phase Diagram and Oxygen-Vacancy Ordering in the Ceo2-Gd2o3 System: A Theoretical Study, Phys Chem Chem Phys 20(17) (2018) 11805-11818.
[56] Y.F. Wang, C.M. Fan, H. Wang, F. Wang, J.M. Xu, P.P. Duan, Y. Zhang, Effects of Tio2 on the Sintering Densification of Uo2-Gd2o3 Burnable Poison Fuel, Ceram Int 41(8) (2015) 10185-10191.

[57] S. Fukushima, T. Ohmichi, A. Maeda, H. Watanabe, The Effect of Gadolinium Content on the Thermal-Conductivity of near-Stoichiometric (U,Gd)O2 Solid-Solutions, J Nucl Mater 105(2-3) (1982) 201-210.
[58] C. Miyake, M. Kanamaru, S. Imoto, Microcharacterization of Gadolinium in U1-Xgdxo2 by Means of Electron-Spin-Resonance, J Nucl Mater 137(3) (1986) 256-260.
[59] M. Hirai, Thermal-Diffusivity of Uo2-Gd2o3 Pellets, J Nucl Mater 173(3) (1990) 247-254.
[60] H. Assmann, M. Peehs, H. Roepenack, Survey of Binary Oxide Fuel Manufacturing and Quality-Control, J Nucl Mater 153 (1988) 115-126.
[61] H.G. Riella, M. Durazzo, M. Hirata, R.A. Nogueira, Uo2-Gd2o3 Solid-Solution Formation from Wet and Dry Processes, J Nucl Mater 178(2-3) (1991) 204-211.
[62] K.W. Song, K.S. Kim, J.H. Yang, K.W. Kang, Y.H. Jung, A Mechanism for the Sintered Density Decrease of Uo2-Gd2o3 Pellets under an Oxidizing Atmosphere, J Nucl Mater 288(2-3) (2001) 92-99.
[63] M. Durazzo, H.G. Riella, Effect of Mixed Powder Homogeneity on the Uo2-Gd2o3 Nuclear Fuel Sintering Behavior, Key Eng Mat 189-1 (2001) 60-66.
[64] V. Tyrpekl, M. Naji, M. Holzhauser, D. Freis, D. Prieur, P. Martin, B. Cremer, M. Murray-Farthing, M. Cologna, On the Role of the Electrical Field in Spark Plasma Sintering of Uo2+X, Sci Rep-Uk 7 (2017).
[65] E.K. Papynov, O.O. Shichalin, A.Y. Mironenko, I.G. Tananaev, V.A. Avramenko, V.I. Sergienko, Uo2 Fuel Pellets Fabrication Via Spark Plasma Sintering Using Non-Standard Molybdenum Die, International Conference on Mechanical Engineering and Applied Composite Materials 307 (2018).
[66] L. Balice, M. Cologna, F. Audubert, J.-L. Hazemann, Densification Mechanisms of Uo2 Consolidated by Spark Plasma Sintering, J Eur Ceram Soc (2020).
[67] E.K. Papynov, O.O. Shichalin, A.A. Belov, A.S. Portnyagin, I.Y. Buravlev, V.Y. Mayorov, A.E. Sukhorada, E.A. Gridasova, A.D. Nomerovskiy, V.O. Glavinskaya, I.G. Tananaev, V.I. Sergienko, Spark Plasma Sintering of Uo2 Fuel Composite with Gd2o3 Integral Fuel Burnable Absorber, Nucl Eng Technol 52(8) (2020) 1756-1763.
[68] M. Durazzo, A.M. Saliba-Silva, E.F.U. De Carvalho, H.G. Riella, Sintering Behavior of Uo2-Gd2o3 Fuel: Pore Formation Mechanism, J Nucl Mater 433(1-3) (2013) 334-340.
[69] M. Durazzo, A.M. Saliba-Silva, E.F.U. De Carvalho, H.G. Riella, Remarks on the Sintering Behavior of Uo2-Gd2o3 Fuel, J Nucl Mater 405(2) (2010) 203-205.
[70] M. Hirai, Et.Al., Young's Modulus of Gd2o3-Uo2, Nb2o5-Uo2 and Tio2-Uo2 Pellets, Fall Meeting of Japan Atomic Energy Society, Japan Atomic Energy Society, Japan, 1991.
[71] R.J. Forlano, A.W. Allen, R.J. Beals, Elasticity and Anelasticity of Uranium Oxides at Room Temperature .I. Stoichiometric Oxide, J Am Ceram Soc 50(2) (1967) 93-&.
[72] J. Fink, M. Chasanov, L. Leibowitz, Thermophysical Properties of Uranium Dioxide, J Nucl Mater 102(1-2) (1981) 17-25.
[73] L.T. Leite, M.S. Dias, Evaluation of the Elastic Constants of the High Burnup Nuclear Fuel (U1-Y,Gdy)O2, 2011 International Nuclear Atlantic Conference, ASSOCIAÇÃO BRASILEIRA DE ENERGIA NUCLEAR, Belo Horizonte,MG, Brazil, 2011.
[74] S. Yamanaka, K. Kurosaki, M. Katayama, J. Adachi, M. Uno, T. Kuroishi, M. Yamasaki, Thermal and Mechanical Properties of (U,Er)O-2, J Nucl Mater 389(1) (2009) 115-118.
[75] M. Hirai, S. Ishimoto, Thermal Diffusivities and Thermal-Conductivities of Uo2-Gd2o3, J Nucl Sci Technol 28(11) (1991) 995-1000.

[76] K. Iwasaki, T. Matsui, K. Yanai, R. Yuda, Y. Arita, T. Nagasaki, N. Yokoyama, I. Tokura, K. Une, K. Harada, Effect of Gd2o3 Dispersion on the Thermal Conductivity of Uo2, J Nucl Sci Technol 46(7) (2009) 673-676.
[77] A. Chotard, P. Melin, M. Bruet, B. Francois, Out of Pile Physical Properties and in Pile Thermal Conductivity of (U, Gd)O2 (Iwgfpt--26), in: I.a.E.A. (Iaea) (Ed.) SPECIFIC NUCLEAR REACTORS AND ASSOCIATED PLANTS (E3200), CEA Framatome, International Atomic Energy Agency (IAEA), 1987, pp. 1-134.
[78] T. Thornton, Et.Al., Thermal Conductivity of Sintered Urania-Gadolinia, ANS Winter Meeting, The American Nuclear Society, Washington, D.C., 1982, pp. 348-349.
[79] R. Skogen, M. Killgore, Performance of Exxon Nuclear Gadolinia-Bearing Fuel in Pressurized Water Reactors, American Nuclear Safety Topical Meeting on Light Water Reactor Fuel Performance, The American Nuclear Society, Orlando, FL, 1985, pp. 5-43 to 5-49.
[80] Y.S. Tishchenko, S.M. Lakiza, V.P. Red'ko, L.M. Lopato, Isothermal Sections of the Al2o3-Hfo2-Er2o3 Phase Diagram at 1250 and 1600 Degrees C, Powder Metall Met C+ 51(9-10) (2013) 594-601.
[81] M. Foex, J.P. Traverse, Etude Du Polymorphisme Des Sesquioxydes De Terres Rares a Haute Temperature, B Soc Fr Mineral Cr 89(2) (1966) 184-&.
[82] O.R. Andrievskaya, O.A. Korniienko, O.I. Bykov, A.V. Sameliuk, Z.D. Bohatyriova, Interaction of Ceria and Erbia in Air within Temperature Range 1500-600 Degrees C, J Eur Ceram Soc 40(8) (2020) 3098-3103.
[83] O.A. Kornienko, A.V. Sameljuk, O.I. Bykov, Y.V. Yurchenko, A.K. Barshchevskaya, Phase Relation Studies in the Ceo2–La2o3–Er2o3 System at 1500°C, J Eur Ceram Soc 40(12) (2020) 4184-4190.
[84] F. Genel, L.K. Podda, D. Minichelli, Solid Solutions in Ternary Phase Diagram Ceo2-Zro2-Er2o3 Using Pyrolitic Precursors, Brit Ceram T 100(4) (2001) 155-158.
[85] A.E.S. Sansone, H.G. Riella, E.F.U.D. Carvalho, Characterization of Crystalline Phases of (U,Er)O2 Pellets by X-Ray Diffraction, 2017 International Nuclear Atlantic Conference, ASSOCIAC¸ AO BRASILEIRA DE ENERGIA NUCLEAR, Belo Horizonte, MG, Brazil, 2017, pp. 1-9.
[86] M. Durazzo, A.C. Freitas, A.E.S. Sansone, N.a.M. Ferreira, E.E.U. De Carvalho, H.G. Riella, R.M.L. Neto, Sintering Behavior of Uo2-Er2o3 Mixed Fuel, J Nucl Mater 510 (2018) 603-612.
[87] H.X. Xiao, C.S. Long, X.M. Wang, H.S. Chen, S.H. Fan, C. Yu, G.L. Liu, Microstructure and Thermophysical Properties of Er2o3-Doped Uo2 Ceramic Pellets, J Nucl Mater 534 (2020).
[88] L.N. Grossman, J.E. Lewis, D.M. Rooney, The System Uo2-Eu2o3 at High Temperatures, J Nucl Mater 21 (1967) 302-309.
[89] T. Kubota, Takahash.S, Behavior of Several Rare Earth Metal Oxide Dispersions in Uo2 at High Temperature, J Nucl Sci Technol-T 4(4) (1967) 171-&.
[90] E.K. Papynov, O.O. Shichalini., Y. Buravlev, A.S. Portnyagin, V.Y. Mayorov, A.A. Belov, A.E. Sukhorada, E.A. Gridasovai, I.G. Tananaev, V.I. Sergienko, Uo2-Eu2o3 Compound Fuel Fabrication Via Spark Plasma Sintering, J Alloy Compd (2020).
[91] W.K. Anderson, J.S. Theilacker, U.S.a.E.C.D.O.R. Development, Neutron Absorber Materials for Reactor Control, Naval Reactors, Division of Reactor Development, U.S. Atomic Energy Commission1962.
[92] G.J.K. Harrington, G.E. Hilmas, W.G. Fahrenholtz, Effect of Carbon on the Thermal and Electrical Transport Properties of Zirconium Diboride, J Eur Ceram Soc 35(3) (2015) 887-896.

[93] J.W. Zimmermann, G.E. Hilmas, W.G. Fahrenholtz, R.B. Dinwiddie, W.D. Porter, H. Wang, Thermophysical Properties of Zrb2 and Zrb2-Sic Ceramics, J Am Ceram Soc 91(5) (2008) 1405-1411.
[94] W. Chubb, Coating a Uranium Dioxide Nuclear Fuel with a Zirconium Diboride Burnable Poison, Westinghouse Electric Corp. (Pittsburgh, PA), United States, 1986.
[95] H.W. Huang, X.M. Wang, J. Yang, K. Xu, S.P. Dai, Effect of Carbide on Al2o3/B4c Burnable Poison Sintered in Ar, Nucl Eng Des 241(12) (2011) 4909-4912.
[96] F. Dannucci, E.B.S. Pardue, W. Rommelaere, G. Baro, Tritium Analysis of Irradiated Burnable Poison Rods, Nucl Technol 59(1) (1982) 9-13.
[97] P. Hofmann, M. Markiewicz, J. Spino, Chemical Interactions between Al2o3, Which Is Used in Burnable Poison Rods, and Zircaloy-4 up to 1500-Degrees-C, J Nucl Mater 166(3) (1989) 287-299.
[98] Y.P. Varshni, Temperature Dependence of the Elastic Constants, Phys Rev B-Solid St 2(10) (1970) 3952-3958.
[99] W.D.C. Jr., D.G. Rethwisch, Fundamentals of Materials Science and Engineering, 5 ed., John Wiley & Sons2018.
[100] L.H. Ortega, B.J. Blamer, J.A. Evans, S.M. Mcdeavitt, Development of an Accident-Tolerant Fuel Composite from Uranium Mononitride (Un) and Uranium Sesquisilicide (U-3 Si-2) with Increased Uranium Loading, J Nucl Mater 471 (2016) 116-121.
[101] J. J. B. Wachtman, Elastic Deformation of Ceramics and Other Refractory Materials, in: J. J. B. Wachtman (Ed.) Mechanical and Thermal Properties of Ceramics, Institute for Materials Research, National Bureau of Standards, Gaithersburg, Maryland, 1968, pp. 139-168.
[102] J.A. Haglund, O. Hunter, Elastic Properties of Polycrystalline Monoclinic Gd2o3, J Am Ceram Soc 56(6) (1973) 327-330.
[103] W.R. Manning, O. Hunter, Elastic Properties of Polycrystalline Yttrium Oxide, Holmium Oxide, and Erbiun Oxide - High-Temperature Measurements, J Am Ceram Soc 52(9) (1969) 492-&.
[104] O. Hunter, H.J. Korklan, R.R. Suchomel, Elastic Properties of Polycrystalline Monoclinic Sm2o3, J Am Ceram Soc 57(6) (1974) 267-268.
[105] V.V. Skripnyak, V.A. Skripnyak, Predicting the Mechanical Properties of Ultra-High Temperature Ceramics, Lett Mater 7(4) (2017) 407-411.
[106] J.K. Fink, Thermophysical Properties of Uranium Dioxide, J Nucl Mater 279(1) (2000) 1-18.
[107] A.T. Biehl, R. Fayram, R. Henley, G.A. Linenberger, H. Montgomery, R. Mainhardt, G. Newby, J. Randall, D. Sawle, J. Sherwin, Compact, Low-Cost Reactor Emphasizes Safety, Nucleonics 14(9) (1956) 100-103.
[108] H.A. R, W.L. Kolb, D.H. Lennox, Engineering, Construction and Cost of the Argonaut Reactor, in: R.E. Division (Ed.) ARGONNE NATIONAL LABORATORY, Lemont, Illinois, 1957.
[109] International Atomic Energy Agency, Research Reactor Database, 2021. https://nucleus.iaea.org/rrdb/#/home. (Accessed Dec. 23 2021).
[110] W. Peiman, I.L. Pioro, K. Gabriel, M. Hosseiny, Handbook of Generation Iv Nuclear Reactors, Elsevier Ltd.2016.
[111] D. Olander, E. Greenspan, H.D. Garkisch, B. Petrovic, Uranium-Zirconium Hydride Fuel Properties, Nucl Eng Des 239(8) (2009) 1406-1424.

[112] D.R. Olander, M. Ng, Hydride Fuel Behavior in Lwrs, J Nucl Mater 346(2-3) (2005) 98-108.
[113] Power Reactor Technology, United States Atomic Energy Commission 1(2) (1958).
[114] J.R. Huffman, D.R. Deboisblanc, J.E. Evans, L.A. Schmittroth, Materials Testing Reactor - Engineering Test Reactor: Technical Branches Quarterly Report, October 1 - December 31,1960, Ido-16665, AEC Research and Development Report (1961).
[115] H. Horiguchi, Safety of Experimental Facility in Jrr-3, Regional Workshop on the Application of the Code of the Conduct on the Safety Research Reactors, International Atomic Energy Agency and National Nuclear Energy Agency, Yogyakarta, Indonesia, 23–27 September 2013.
[116] R. Mudau, D. Botes, F.a.V. Heerden, Numerical Modelling of Control Rod Calibrations and Fuel Depletion at the Opal Research Reactor, Proceedings of SAIP2017, 62nd Annual Conference of the South African Institute of Physics, Stellenbosch University, Stellenbosch, South Africa, 3-7 July 2017.
[117] J.M.Tuñón, E.A.Villarino, D. Ferraro, P. Camusso, G. Sarabia, F.Sánchez, Neutronic Design of the Ra10 Research Reactor´S Core, 16th meeting of the International Group On Research Reactors (IGORR 2014), Bariloche, Argentina, 2014.
[118] E. Villarino, F. Leszczynski, Numerical Benchmarks for Mtr Fuel Assemblies with Burnable Poison, 18th meeting of the International Group On Research Reactors (IGORR 2017), Syndney, Australia, 2017.
[119] S.S. Kim, B.G. Schnitzler, Advanced Test Reactor: Serpentine Arrangement of Highly Enriched Water-Moderated Uranium-Aluminide Fuel Plates Reflected by Beryllium, NEA/NSC/DOC/(95)03/II, Volume II, HEU-MET-THERM-022.
[120] G. Beckman, R. Kiessling, Thermal Expansion Coefficients for Uranium Boride and Beta-Uranium Silicide, Nature 178(4546) (1956) 1341-1341.
[121] B.J. Mcdonald, W.I. Stuart, The Crystal Structures of Some Plutonium Borides, Acta Crystallogr 13(5) (1960) 447-448.
[122] E. Jossou, D. Oladimeji, L. Malakkal, S. Middleburgh, B. Szpunar, J. Szpunar, First-Principles Study of Defects and Fission Product Behavior in Uranium Diboride, J Nucl Mater 494 (2017) 147-156.
[123] E. Kardoulaki, J.T. White, D.D. Byler, D.M. Frazer, A.P. Shivprasad, T.A. Saleh, B. Gong, T. Yao, J. Lian, K.J. Mcclellan, Thermophysical and Mechanical Property Assessment of Ub2 and Ub4 Sintered Via Spark Plasma Sintering, J Alloy Compd 818 (2020).
[124] K. Matterson, H. Jones, A Study of the Tetraborides of Uranium and Thorium, Transactions of the British Ceramic Society 60 (1961).
[125] P.A. Burr, E. Kardoulaki, R. Holmes, S.C. Middleburgh, Defect Evolution in Burnable Absorber Candidate Material: Uranium Diboride, Ub2, J Nucl Mater 513 (2019) 45-55.
[126] D. Frazer, B. Maiorov, U. Carvajal-Nunez, J. Evans, E. Kardoulaki, J. Dunwoody, T.A. Saleh, J.T. White, High Temperature Mechanical Properties of Fluorite Crystal Structured Materials (Ceo2, Tho2, and Uo2) and Advanced Accident Tolerant Fuels (U3si2, Un, and Ub2), J Nucl Mater 554 (2021).
[127] K.Y. Spencer, L. Sudderth, R.A. Brito, J.A. Evans, C.S. Hart, A.B. Hu, A. Jati, K. Stern, S.M. Mcdeavitt, Sensitivity Study for Accident Tolerant Fuels: Property Comparisons and Behavior Simulations in a Simplified Pwr to Enable Atf Development and Design, Nucl Eng Des 309 (2016) 197-212.

[128] D.A. Lopes, S. Uygur, K. Johnson, Degradation of Un and Un-U3si2 Pellets in Steam Environment, J Nucl Sci Technol 54(4) (2017) 405-413.
[129] E.S. Wood, J.T. White, C.J. Grote, A.T. Nelson, U3si2 Behavior in H2o: Part I, Flowing Steam and the Effect of Hydrogen, J Nucl Mater 501 (2018) 404-412.
[130] A.T. Nelson, A. Migdisov, E.S. Wood, C.J. Grote, U3si2 Behavior in H2o Environments: Part Ii, Pressurized Water with Controlled Redox Chemistry, J Nucl Mater 500 (2018) 81-91.
[131] J. Turner, S. Middleburgh, T. Abram, A High Density Composite Fuel with Integrated Burnable Absorber: U3si2-Ub2, J Nucl Mater 529 (2020).
[132] E. Jossou, L. Malakkal, B. Szpunar, D. Oladimeji, J.A. Szpunar, A First Principles Study of the Electronic Structure, Elastic and Thermal Properties of Ub2, J Nucl Mater 490 (2017) 41-48.
[133] J.T. White, A.T. Nelson, J.T. Dunwoody, D.D. Byler, D.J. Safarik, K.J. Mcclellan, Thermophysical Properties of U3si2 to 1773 K, J Nucl Mater 464 (2015) 275-280.
[134] W. Köster, H. Franz, Poisson's Ratio for Metals and Alloys, Metallurgical Reviews 6(1) (1961).
[135] K.D. Johnson, A.M. Raftery, D.A. Lopes, J. Wallenius, Fabrication and Microstructural Analysis of Un-U3si2 Composites for Accident Tolerant Fuel Applications, J Nucl Mater 477 (2016) 18-23.
[136] J. Turner, J. Buckley, G. Phillips, T.J. Abram, The Use of Gadolinium as a Burnable Poison within U3si2 Fuel Pellets, J Nucl Mater 509 (2018) 204-211.
[137] S.L. Hayes, J.K. Thomas, K.L. Peddicord, Material Property Correlations for Uranium Mononitride .2. Mechanical-Properties, J Nucl Mater 171(2-3) (1990) 271-288.
[138] Z.Y. Fu, I.J. Van Rooyen, M. Bachhav, Y. Yang, Microstructure and Fission Products in the Uco Kernel of an Agr-1 Triso Fuel Particle after Post Irradiation Safety Testing, J Nucl Mater 528 (2020).
[139] P. Trinuruk, T. Obara, Small, Long-Life High Temperature Gas-Cooled Reactor Free from Prompt Supercritical Accidents by Particle-Type Burnable Poisons, J Nucl Sci Technol 50(9) (2013) 898-912.
[140] J.L. Kloosterman, H. Van Dam, T.H.J.J. Van Der Hagen, Applying Burnable Poison Particles to Reduce the Reactivity Swing in High Temperature Reactors with Batch-Wise Fuel Loading, Nucl Eng Des 222(2-3) (2003) 105-115.
[141] T. Obara, T. Onoe, Flattening of Burnup Reactivity in Long-Life Prismatic Htgr by Particle Type Burnable Poisons, Ann Nucl Energy 57 (2013) 216-220.
[142] C.K. Jo, Y. Kim, J.M. Noh, Burnable Poison for Reactivity Management in a Very High Temperature Reactor, Ann Nucl Energy 36(3) (2009) 298-304.
[143] P. Trinuruk, T. Obara, Particle-Type Burnable Poisons for Thorium-Based Fuel in Htgr, Enrgy Proced 71 (2015) 22-32.
[144] M. Kauchi, Y. Shimazu, Optimal Burnable Poison-Loading in a Pwr with Carbon Coated Particle Fuel, J Nucl Sci Technol 40(1) (2003) 22-29.
[145] J. Washington, J. King, Z. Shayer, Selection and Evaluation of Potential Burnable Absorbers Incorporated into Modified Triso Particles, Nucl Eng Des 278 (2014) 377-386.
[146] J. Guidez, L. Martin, G. Giraud, J. Sauvage, Summary of the Operation of Sodium-Cooled Fast Reactors Throughout the World, Rgn No. 3, 2010.
[147] H. Guo, L. Buiron, P. Sciora, T. Kooyman, Optimization of Reactivity Control in a Small Modular Sodium-Cooled Fast Reactor, Nucl Eng Technol 52(7) (2020) 1367-1379.

[148] H. Guo, P. Sciora, T. Kooyman, L. Buiron, G. Rimpault, Application of Boron Carbide as Burnable Poison in Sodium Fast Reactors, Nucl Technol 205(11) (2019) 1433-1446.
[149] E. Teller, M. Ishikawa, L. Wood, Completely Automated Nuclear Reactors for Long-Term Operation, Frontiers in Physics Symposium, American Physical Society and American Association of Physics Teachers Texas Meeting, Lubbock, Texas, 1995.
[150] H. Van Dam, Self-Stabilizing Criticality Waves, Ann Nucl Energy 27(16) (2000) 1505-1521.
[151] H.V. Dam, The Self-Stabilizing Criticality Wave Reactor, Tenth International Conference on Emerging Nuclear Energy Systems, NRG, Petten, Netherlands, 2000, pp. 188-197.
[152] Y.I. Chang, P.J. Finck, C. Grandy, Advanced Burner Test Reactor Preconceptual Design Report, Anl-Abr-1 (Anl-Afci-173), Usdoe Office of Science, 2006.
[153] C. Grandy, R. Seidensticker, Advanced Burner Reactor 1000mwth Reference Concept, Anl-Afci-202 (Anl-Abr-4), Usdeo Office of Science, 2007.